CMOS Integrated Optics

Studies on Submicron Waveguide Mode Properties and Devices

Amit Khanna

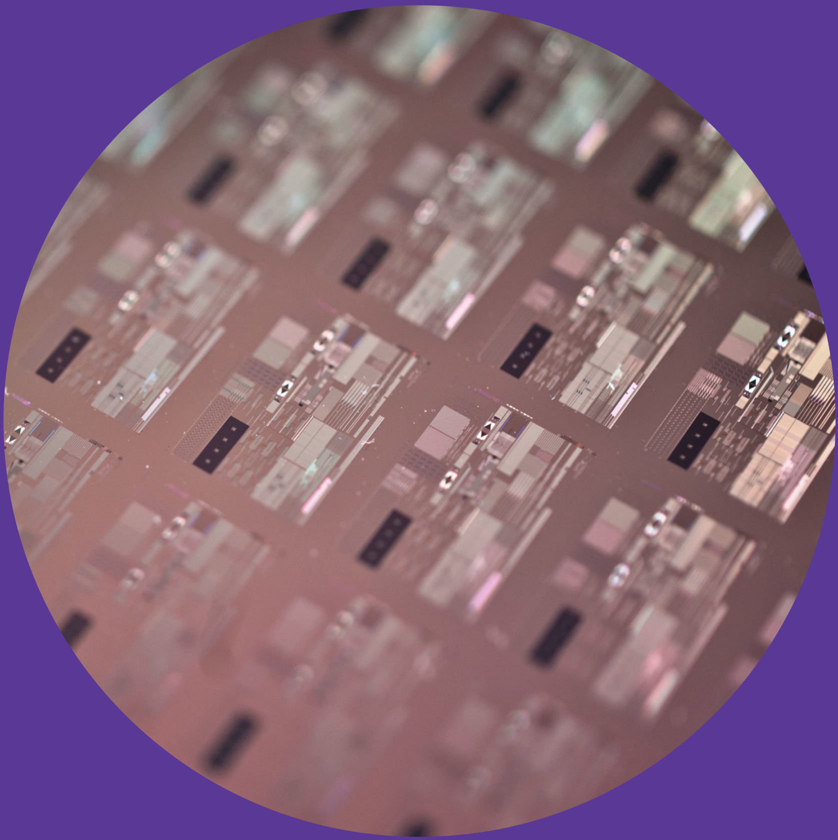

Aalto University

DOCTORAL
DISSERTATIONS

Aalto University publication series
DOCTORAL DISSERTATIONS 74/2015

CMOS Integrated Optics

Studies on Submicron Waveguide Mode Properties and Devices

Amit Khanna

A doctoral dissertation completed for the degree of Doctor of Science (Technology) to be defended, with the permission of the Aalto University School of Electrical Engineering, at a public examination held at the lecture hall AS2 of the TUAS Building (Otaniementie 17, Espoo, Finland) of the school on 5 June 2015 at 12.

Aalto University
School of Electrical Engineering
Department of Micro and Nanosciences
Nanotechnology Group

Supervising professor
Harri Lipsanen, Seppo Honkanen

Thesis advisor
Antti Saynatjoki

Preliminary examiner
Dr. Stefano Pelli (CNR, Italy), Dr. Jussi Hiltunen (VTT, Finland)

Opponent
Dr. Andrea Melloni (Professor), Politecnico di Milano, Italy

Aalto University publication series
DOCTORAL DISSERTATIONS 74/2015

ISBN 978-952-60-6224-2 (printed)
ISBN 978-952-60-6225-9 (pdf)
ISSN-L 1799-4934
ISSN 1799-4934 (printed)
ISSN 1799-4942 (pdf)
http://urn.fi/URN:ISBN:978-952-60-6225-9

Unigrafia Oy
Helsinki 2015

Finland

NORDIC ECOLABEL
441 697
Printed matter

Aalto University

Abstract

Aalto University, P.O. Box 11000, FI-00076 Aalto www.aalto.fi

Author
Amit Khanna

Name of the doctoral dissertation
CMOS Integrated Optics: Studies on Submicron Waveguide Mode Properties and Devices

Publisher School of Electrical Engineering

Unit Department of Micro and Nanosciences

Series Aalto University publication series DOCTORAL DISSERTATIONS 74/2015

Field of research Integrated Optics, CMOS Photonics

Manuscript submitted 25 September 2014 **Date of the defence** 5 June 2015

Permission to publish granted (date) 7 January 2015 **Language** English

☐ **Monograph** ☒ **Article dissertation (summary + original articles)**

Abstract

The aim of this thesis is to demonstrate novel or improved photonic devices based on the CMOS based photonics processes. Methods to obtain application-specific optical mode characteristics through design, fabrication and post-processing are proposed. Focus is on devices attainable within the capabilities of 130 nm CMOS node tool-set, thereby ensuring manufacturability of photonic devices studied in this thesis.

Compared to the widely studied 1D polarization sensitive slot waveguides, we demonstrate novel designs for 2D slot waveguides with high confinement for both polarizations of the fundamental optical mode (quasi-TE and quasi-TM). It is shown that on the basis of required optical mode characteristics such as effective index, birefringence, confinement and mode overlap; cross-slot waveguide, closed 2D slot waveguide, open 2D slot waveguide or u-slot waveguide can be used. It is also shown that angled sidewall in vertical slot waveguide aides void-less filling of the narrow vertical slot waveguide and enhances interaction with the non-linear slot. Asymmetric vertical slot waveguides to achieve non-reciprocal phase shift are also discussed. Furthermore, unprecedented reduction of optical propagation loss is demonstrated for the shorter wavelength regime (980 nm) in the CMOS based silicon nitride material system. This is realized through CMOS compatible ALD based wafer-scale post-processing technique.

Keywords integrated optics, photonics, waveguide, nanophotonics, silicon photonics, CMOS photonics, waveguides, slot waveguide,

ISBN (printed) 978-952-60-6224-2 **ISBN (pdf)** 978-952-60-6225-9

ISSN-L 1799-4934 **ISSN (printed)** 1799-4934 **ISSN (pdf)** 1799-4942

Location of publisher Helsinki **Location of printing** Helsinki **Year** 2015

Pages 114 **urn** http://urn.fi/URN:ISBN:978-952-60-6225-9

Preface

I was first introduced to silicon photonics during an internship at Sterlite Opticals in 2005. Micrometer sized light guiding devices were of much interest to me [1]. Under the supervision of Dr. Mikaël Mulot, a Master's thesis in silicon photonics in 2007-08 was instrumental in giving direction and providing hands-on experience with nano-devices. Then onwards various people gave a strong fillip to this thesis. Firstly, Professor Seppo Honkanen, who accepted me as a researcher in his Photonics Group. His advice and encouragement is a constant source of inspiration. To Docent Ari Tervonen, I owe great debt for sharing his knowledge and insight on optical devices built over decades of experience, until I was satisfied. Docent Antti Säynätjoki, for sharing my enthusiasm on the subject. His balancing act of pulling-out and letting-swim *these waters* was deft. Professor Roel Baets, my former manager at imec, for reminding me of the unfulfilled thesis and its importance. And not least my wife, Geetika, for her patience and constant support.

I am grateful to Professor Harri Lipsanen for extending all help and ensuring I engage with Aalto University while being fully absorbed in the industry. I also thank Professor Robert A. Norwood for hosting my visit to the College of Optical Sciences, University of Arizona, USA. My mentor at College of Optical Sciences, Dr. Palash Gangopadhyay who instilled a strong work ethic while providing a glimpse of the world of nano-composites. Aalto University courses have been instrumental to my research work. Courses such as integrated optics by Dr. Seppo Honkanen, new venture development by Dr. Peter Kelly and nanotechnology by Dr. Babak Parviz and Dr. Harri Lipsanen were excellent. I am also grateful to the team of the FP7 HELIOS project for organizing the CMOS Photonics winter school at University of Trento in 2009. It was inspiring to hear Professors Lorenzo Pavesi, Danxia Xu, Wim Bogaerts and Entrepreneur Dr. Cary Gunn within a week. Over these years I had the opportunity to meet various scientists and colleagues many of whom became good friends. I have been fortunate to share work space, many light moments and strong *musta kahvi* with Ya Chen, Gintare Statkute, Päivi Mattila, Lasse Karvonen, Joan J. Montiel í Ponsoda, Henri Jussila, Alex

Pyymäki Perros, Nagarajan Subramaniam, Nikolai Chekurov, Muhammad Ali, Tapani Alasaarela, and Ananth Z. Subramanian.

I am grateful to my parents, Lalit and Rashmi, and all teachers from various stages of learning; for their care and nurture. I also thank my friends for being there and hopefully for long, SachinC, Pavan, Cathy, László, Judith, Varun, Kumar, Pardip, SachinG, Bahram and Kuldeep. I would also like to acknowledge the Elisa Foundation for their recognition of this thesis work in 2010. The GETA foundation for sponsoring the thesis work and excellent doctoral courses from 2010-2012. Academy of Finland, Tekes and the Inspectra Project of the Flemish research council for funding the projects enabling our research work.

Antwerp, Belgium, May 19, 2015,

Amit Khanna

Contents

List of Publications

This thesis consists of an overview and of the following publications which are referred to in the text by their Roman numerals.

I Khanna Amit, Säynätjoki Antti, Tervonen Ari, Honkanen Seppo. Control of Optical Mode Properties in Cross-slot Waveguides. *Applied Optics*, Volume 48, Number 34, pages 6547-6552, December 2009.

II Khanna Amit, Säynätjoki Antti, Tervonen Ari, Norwood Robert A., Honkanen Seppo. Polarization Properties of Two-Dimensional Slot Waveguides. *Applied Optics*, Volume 49, Number 28, pages 5321-5332, October 2010.

III Säynätjoki Antti, Alasaarela Tapani, Khanna Amit, Karvonen Lasse, Stenberg Petri, Kuittinen Markku, Tervonen Ari, Honkanen Seppo. Advantages of Angled Sidewalls in Slot Waveguides: Conformal Filling and Mode Properties. *Optics Express*, Volume 17, Issue 23, pages 21066-21076, October 2009.

IV Tervonen Ari, Khanna Amit, Säynätjoki Antti, Honkanen Seppo. Modeling Study of Non-reciprocal Phase Shift in Magneto-optic Asymmetric Slot Waveguides. *Journal of Lightwave Technology*, Volume 29, Number 5, pages 656-660, March 2011.

V Khanna Amit, Subramanian Ananth Z, Häyrinen Markus, Selvaraja Shankar, Verheyen Peter, Thourhout Dries Van, Honkanen Seppo, Lipsanen Harri, Baets Roel. Impact of ALD grown passivation layers on silicon nitride based integrated optic devices for very-near-infrared wavelengths. *Optics Express*, Volume 22, Number 5, pages 5684-5692, March 2014.

Author's Contribution

Publication I: "Control of Optical Mode Properties in Cross-slot Waveguides"

The author initiated the study of cross-slot waveguide and contributed to the simulations and the preparation of the manuscript.

Publication II: "Polarization Properties of Two-Dimensional Slot Waveguides"

The author initiated the study of 2D slot waveguides and contributed to the simulations and the preparation of the manuscript.

Publication III: "Advantages of Angled Sidewalls in Slot Waveguides: Conformal Filling and Mode Properties"

The author contributed to the study of optical mode properties of slot waveguides and preparation of the manuscript.

Publication IV: "Modeling Study of Non-reciprocal Phase Shift in Magneto-optic Asymmetric Slot Waveguides"

The author contributed to the study of the optical mode properties of asymmetric slot waveguides and preparation of the manuscript.

Publication V: "Impact of ALD grown passivation layers on silicon nitride based integrated optic devices for very-near-infrared wavelengths"

The author initiated the research collaboration between Ghent University, Aalto University and University of Eastern Finland for this research.

The author contributed to design of experiment, measurements, simulations and preparation of the manuscript.

Acronyms

2D	two dimensional
3D	three dimensional
AFM	atomic force microscopy
ALD	atomic layer deposition
AWG	arrayed waveguide grating
CD	critical dimension
CMOS	complementary metal-oxide-semiconductor
DfM	design for manufacturability
DRC	design rule check
FIB	focussed ion beam
FMM	film mode matching
FOM	figure of merit
GC	grating coupler
LVS	layout versus schematic
MZI	Mach-Zehnder interferometer
NRPS	non-reciprocal phase shift
OPC	optical proximity correction
PDK	process design kit
PECVD	plasma enhanced chemical vapor deposition
RIE	reactive ion etching
RMS	root mean square

SEM	scanning electron microscope
SOI	silicon on insulator
TE	transverse electric
TM	transverse magnetic
TMA	tri-methyl aluminum
TSV	through-silicon-via
VNIR	very near infrared

Latin Symbols

B	magnetic flux density
D	electric displacement
D_m	material dispersion
E	electric field strength
H	magnetic field strength
J	electric current density
Pz	z component of the Poynting vector
T	temperature
TE_{neff}	effective index of the quasi-TE mode
l_b	beat length
l_c	correlation length
$n - type$	semiconductors with excess electron concentration
n_g	group index
n_{eff}	effective index
$p - type$	semiconductors with excess hole concentration
v_c	speed of light in vacuum

Greek Symbols

α_2	nonlinear loss
β	longitudinal propagation constant
T	confinement factor
ϵ_o	absolute dielectric permittivity
θ_F	Faraday rotation in the bulk material
κ	coupling of the two orthogonal polarization modes by Faraday rotation
κ_o	wave vector
λ	wavelength
μ_o	permeability in vacuum
ρ	electric current density
σ	root mean square roughness
ω	angular frequency

1 Introduction

Benefits of complementary metal-oxide-semiconductor (CMOS) processing and integrated photonics combine in silicon photonics. The concept was first proposed by Soref et al. in 1985 [2] and recommended for its advantages to optical interconnects by Miller [3]. Both discussed in detail the benefits of using mature semiconductor processing infrastructure to realize silicon based planar optical waveguide circuits [4], [5]. CMOS processing infrastructure for 200 mm wafers is capable of providing uniform device performance across the wafer. Furthermore, step-and-scan lithography systems ensure high fidelity of devices and circuits, allowing device designers to design dimensions down to 100 nm in linewidth [6]. CMOS processing makes it possible to realize technologies with very high throughput and yield, thus enabling them to benefit from economics of scaling. Due to material transparency of bulk silicon to infra-red wavelengths, it can be used as an optical waveguide, the most fundamental integrated optics device [7]. Furthermore, other basic integrated optics devices such as splitters, couplers, resonators, waveguides etc. can be realized. The refractive index (n) of silicon at 1.55 μm wavelength is $\sim$3.5. When surrounded by air (n=1) or SiO_2 (n=1.46), silicon provides very high index contrast to guided light. The high index contrast enables strong confinement of light into small waveguide cross-sections. Therefore, narrow waveguide cross-section ($\sim$0.1 μm sq.) can be used to guide light, and, adjacent waveguides can be located proximal (<2 μm) with minimal cross-talk [8]. The high mode confinement also enables compact bends ($\sim$3 μm bend radii) [9]. Together, these aspects allow extremely compact photonic circuits. Fig. 1.1 shows a 200 mm silicon photonics wafer typically comprising dense waveguide circuits. The cross-section of the waveguide also shows the guided optical mode which can have high confinement.

Active functions can also be realized in silicon photonics. This is enabled by factor of twenty difference in thermo-optic coefficients of Si and SiO_2 [10]. Thermo-optic effect is useful to actively tune the performance of photonic circuits. However, the thermo-optic effects cannot reach GHz range. For faster modulation, carrier plasma based dispersion effect can be used. Plasma dispersion can be invoked by applying external elec-

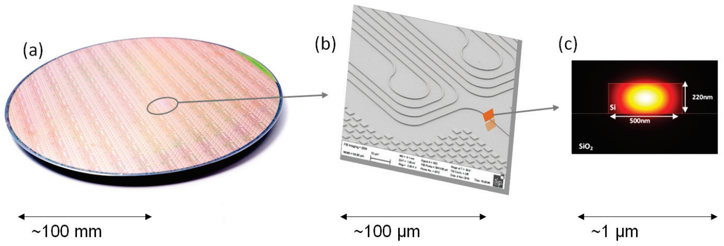

Figure 1.1: (a) 200 mm silicon photonics wafer, *image source: imec, Belgium*. (b) Silicon photonics circuit with spirals, *image source: IHP, Germany*. (c) Optical mode field distribution of an optical waveguide.

tric field to vary charge distribution across p-n junctions formed in silicon by $n-type$ or $p-type$ dopants introduced through conventional CMOS ion implantation process [11]. Furthermore, germanium epitaxial growth has been demonstrated on top of crystalline silicon to realize infra-red detectors [12]. Finally, silicon photonics processing within a CMOS line facilitates the integration with electronics. This has been shown monolithically by commercial foundries [13]. Further, an alternate monolithic approach with SiGe bi-CMOS integration is also being investigated [14]. It is also possible to integrate silicon photonic dies with electronic dies through flip-chip bonding or three dimensional (3D) integration, for example by through-silicon-via (TSV) technology. Therefore, silicon photonics is enabled by nanoelectronic infrastructure and promises to enable nanoelectronics for *More-(of)-Moore*[1] and *More-than-Moore*[2] requirements.

Although these reasons are promising to pursue photonic integration in silicon, it is important to realize some of its pertinent challenges. These include, achieving low insertion loss to sub-micrometer waveguides, low propagation loss within waveguides, on-chip silicon photonic isolator, lasing in silicon etc. Finding a solution to these limitations requires an in-depth understanding of guided mode field distribution to enable sufficient overlap with active regions or high confinement within silicon. A change from target silicon thickness by 1 nm or waveguide width by 2 nm results in $\sim$1 nm spectral shift in the performance of a basic ring resonator in silicon photonics [16]. Thus, GHz range channel spacing in optical fiber based telecommunication infrastructure, poses a severe challenge to even the

---

[1] ’More-(of)-Moore’ refers to further scaling of silicon CMOS technology [15].

[2] ’More-than-Moore’ refers to the integration of non-digital or new functionalities with silicon CMOS through heterogeneous integration [15].

robust electronic manufacturing infrastructure, simultaneously affirming the relevance of extreme process control in silicon photonics. In this thesis, we study the effect of mode field distributions on fundamental properties of optical waveguides in CMOS photonics, such as, effective index of the guided light, optical loss during transmission, light confinement and birefringence. Options to vary these fundamental characteristics through design, fabrication or post-processing are proposed and demonstrated. Fabrication related variations are discussed and strategies to reduce fabrication dependence are investigated. We propose various waveguide geometries and their applications, such as thermo-optically tunable waveguides to achieve zero birefringence, magneto-optic effects to realize an optical isolator, optical loss reduction and enhancement of non-linear effects.

2 Planar Optical Waveguides

2.1 Slab mode theory

2.1.1 Analytical solution to slab waveguides based on Maxwell's equations

Dielectric slab waveguides are a simple geometry to analytically study modes within an optical waveguide. It is an important step towards understanding the mode properties of the more complex high confinement dielectric waveguide structures. Guided modes of a slab waveguide are obtained starting from the Maxwell's equations.

$$\bigtriangledown \times E + \frac{\partial B}{\partial t} = 0 \tag{2.1}$$

$$\bigtriangledown \times H - \frac{\partial D}{\partial t} = J \tag{2.2}$$

$$\bigtriangledown \cdot B = 0 \tag{2.3}$$

$$\bigtriangledown \cdot D = \rho \tag{2.4}$$

where E, H, B, D, J and ρ are electric field strength, magnetic field strength, magnetic flux density, electric displacement, electric current density and electric charge density, respectively.

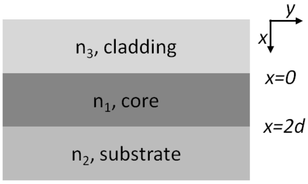

Figure 2.1: Schematic representation of a slab waveguide with core(n_1), substrate(n_2) and cladding (n_3) layers.

Fig. 2.1 shows schematically the slab waveguide cross section. Let us assume core index n_1, substrate index n_2 and top cladding index n_3. The behaviour of the slab waveguide can be understood by assuming the three layer model as shown in the schematic. It is assumed that the waveguide is infinite in y and z directions and has finite thickness 2d in x direction. Such waveguide supports finite number of guided modes. Assuming material of each layer is non-magnetic and isotropic i.e. ϵ_o is scalar, μ=μ_o, D=n^2 ϵ_oE, B=μ_o H, J=0 and ρ=0, substituting these and applying curl on both sides of Eqn. 2.1, the Maxwell's equation can be simplified to,

$$\bigtriangledown^2 E = \mu_o \epsilon_o n_i^2 \frac{\partial^2 E}{\partial t^2}. \tag{2.5}$$

Assuming time harmonic dependence of the electric field E as $e^{-j\omega t}$, where ω is the angular frequency, in phasor representation Eqn. 2.5 can be rewritten as

$$\bigtriangledown^2 E + k_o^2 n_i^2 E = 0 \tag{2.6}$$

where n$_i$ $i \in$ (1,2,3) is the refractive index of the three layers. κ_o is the free space wave number given by $k_o = \omega\sqrt{\epsilon_o \mu_o}$. Electric field E is a phasor quantity with both amplitude and phase. In phasor representation E is function of both space (x, y and z) coordinates and frequency ω. Further assuming a z dependence of E of the form $e^{-j\beta z}$, where β is the longitudinal propagation constant, Eqn. 2.6 can be rewritten as

$$\frac{\partial^2 E}{\partial x^2} + (k_o^2 n_i^2 - \beta^2) E = 0. \tag{2.7}$$

Eqn. 2.7 is known as the *Helmholtz equation*.

The field of a slab waveguide is in general a superposition of the transverse electric (TE) and transverse magnetic (TM) modes. The field component of the two polarizations are H_x, E_y and H_z for TE polarized waves and E_x, H_y and E_z for TM polarized waves. By using Eqn. 2.7 the TE scalar wave equation for the three waveguide regions takes the following form,

$$\frac{\partial^2 E_y}{\partial x^2} - r^2 E_y = 0, x \leq 0 \tag{2.8}$$

$$\frac{\partial^2 E_y}{\partial x^2} + q^2 E_y = 0, 0 \leq x \leq 2d \tag{2.9}$$

$$\frac{\partial^2 E_y}{\partial x^2} - p^2 E_y = 0, x \geq 2d \tag{2.10}$$

where $r^2 = \beta^2 - k_0^2 n_3^2$, $q^2 = k_0^2 n_1^2 - \beta^2$ and $p^2 = \beta^2 - k_0^2 n_2^2$. For guided modes the power should stay confined to the central region of the core. The form of Eqn. 2.8, 2.9 and 2.10 implies that this requirement will be met by an oscillatory solution in the core region and evanescent tails in the cladding and substrate regions. Assuming $n_1 > n_2 \geq n_3$, for guided modes, range of β is given by $k_o n_1 \geq \beta \geq k_o n_2 \geq k_o n_3$. By applying the boundary conditions, continuity of the tangential H_z component at $x = 0$ and $x = 2d$ we obtain the eigen value equation of TE mode for a slab waveguide,

$$\tan(2dq) = \frac{q(p+r)}{q^2 - pr}. \tag{2.11}$$

2.1.2 Effective index

Propagation constant β can be represented as $\beta = k_o n_{eff}$, where n_{eff} is known as the effective index of the guided mode. Due to anisotropicity of material distributions both the polarizations have different n_{eff} values.

2.1.3 Confinement factor

Confinement factor (T) is calculated as,

$$T = \frac{\epsilon_o v_c}{4} \frac{\int^R n_r(s).E^2(s).ds}{\int^\infty P_z(s).ds} \tag{2.12}$$

where numerator is integrated over region *R* and the lower integral is evaluated over the entire cross-section. In the above equation, Pz represents the *z* component of the Poynting vector and v_c, the speed of light in vacuum. Confinement factor of a mode in a certain region R (T_R) is defined such that,

$$\alpha_{mode} = T_R \alpha_R \tag{2.13}$$

where, α_{mode} is the optical mode loss/gain when guided within the waveguide region. α_R is the optical loss/gain per unit length in the bulk region of the same material.

2.2 Waveguide types and properties

As shown in the previous chapter optical slab waveguide supports eigen modes. In silicon photonics, slab-waveguide-like multimode regions are utilized often to design areas of low optical propagation loss, reduce reflections in devices, and allow mode interference in interferometric devices. As an example, arrayed waveguide gratings (AWGs) use multi-mode star coupler regions to transition waveguides from compact strip waveguide to ridge waveguide and finally to arrayed waveguide region. Based on the application waveguide cross-sections of different types can be implemented. In this section we will discuss the most common silicon photonics waveguide cross-sections and their characteristics. Unless mentioned otherwise, most of the optical mode simulations are based on film mode matching (FMM) method, FIMMWAVE software. FMM method is best suitable for rectangular geometries, thin films and vertical sidewalls [17]. The FIMMWAVE tool also facilitates computation of confinement factor and dispersion, thereby allowing analysis of sub-micrometer waveguides mode properties.

2.2.1 Waveguide cross-sections

Choice of the waveguide cross-section is an important aspect of designing silicon photonic circuits. Depending upon the targeted application, different waveguide cross-sections offer more suitable mode characteristics. Such fundamental waveguide mode characteristics are effective index, waveguide loss, mode confinement and birefringence. Simulations are performed using the FMM method to compare the n_{eff} and T of the fundamental TE optical modes of different waveguide geometries. Typically used abbreviations for simulations are, refractive index of silicon (n_{Si}=3.5), refractive index of SiO_2 (n_{SiO2}=1.46) and refractive index of air (n_{air}=1). Standard silicon on insulator (SOI) wafer thickness of 220 nm is used, shallow slab thickness=70 nm, ridge waveguide core width=500 nm, strip waveguide width= 500 nm and height=220 nm, and slot waveguide rail width=300 nm and slot width=100 nm. For slab waveguide simulations perfectly matching layers were used as terminations of the simulation window. For all other geometries the simulation window size is assumed to be sufficiently large (greater than 1 μm wide and 1 μm high) so that the electric-field intensity of the guided fundamental quasi-TE mode is negligible at the simulation window boundaries. All simulations are performed for 1.55 μm wavelength. In Fig. 2.2(a) slab waveguide discussed in the previous section is schematically shown together with the simulated intensity profile of the fundamental quasi-TE mode. For such a waveguide the fundamental quasi-TE mode field intensity spreads across the slab structure and is only bound by the material discontinuity of the top (air) and bottom (SiO_2) claddings. Intensity of the optical mode is maximum within the silicon slab region. Due to material asymmetry the intensity maximum is closer to the bottom cladding. Fig. 2.2(b) shows the schematic of a ridge waveguide. Compared to a slab waveguide the ridge waveguide introduces a material index contrast in the horizontal direction by a partial etch of the 220 nm silicon layer. For the etched region slab height of 150 nm (h) is assumed and the width of the core is assumed to be 500 nm (w). The ridge mode intensity profile is concentrated within the core region and spreads further into the shallower slab region. The waveguide mode results are also highlighted in Table 2.1. The slab waveguide fundamental TE_{neff} is simulated to be 2.86 which is higher than TE_{neff} of the ridge waveguide mode, 2.52. As illustrated in the intensity distributions of the fundamental mode, the T of the slab waveguide is high (0.82). In comparison the studied ridge waveguide geometry has smaller fundamental mode field T (0.76). The reduced T in ridge waveguide is due to greater overlap of the optical mode field with the claddings.

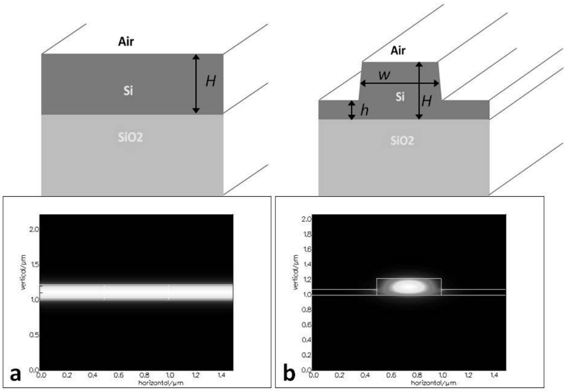

Figure 2.2: Schematic of waveguides with height H and Si as the core region. Bottom cladding is SiO_2 and top cladding is air. Below, intensity plot of fundamental quasi-TE mode for, (a) slab waveguide and, (b) ridge waveguide with ridge height h and core width w.

In Fig. 2.3(a) strip waveguide is shown schematically together with the simulated intensity profile of the supported fundamental quasi-TE mode. The strip waveguide differs from the ridge waveguide in having a complete etch of the slab region adjacent to the core. This introduces high refractive index contrast in the horizontal direction. Standard SOI wafer thickness of 220 nm (H) and waveguide width of 500 nm (w) is used for simulations. For such a waveguide the fundamental quasi-TE mode field intensity distribution is more concentrated than ridge waveguide due to an even higher refractive-index contrast introduced in the horizontal direction due to a complete etch of the silicon layer. Intensity of the fundamental quasi-TE optical mode has a maximum within this core silicon region. Due to material asymmetry, the intensity maxima is closer to the bottom cladding in the vertical direction, but centred (due to symmetry) in the horizontal direction.

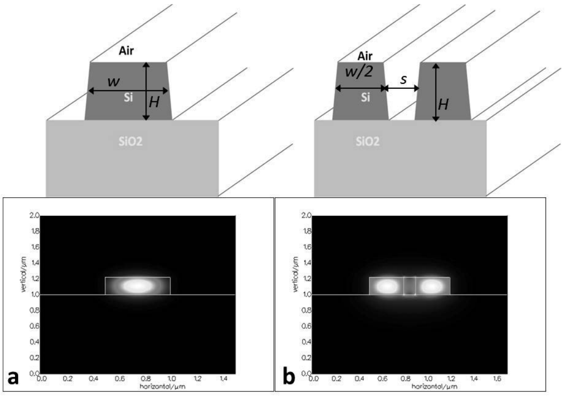

Figure 2.3: Schematic of waveguides with height H and Si as the core region. Bottom cladding is SiO_2 and top cladding is air. Below, intensity plot of fundamental quasi-TE mode for (a) strip waveguide and, (b) slot waveguide.

Fig. 2.3(b) shows the schematic of a slot waveguide. Compared to a strip waveguide the slot waveguide introduces another material discontinuity in the horizontal direction by a complete vertical etch between the silicon core of a strip waveguide. The resultant waveguide is a combination of two adjacent silicon rails separated by a narrow slot region. For simulations of slot waveguide, height of the rails is 220 nm (H), width of the rails is 250 nm ($w/2$) and the slot width (s) 100 nm. Due to the narrow slot region, optical mode field intensity distribution of the fundamental quasi-TE mode of the slot waveguide has a maxima in the low-index slot region. This characteristic of slot waveguide distinguishes it from all previously discussed waveguide cross-sections. Slot waveguide characteristics have been proposed and studied in [18]. The strip waveguide fundamental TE_{neff} is 2.41 which is less than TE_{neff} of the ridge waveguide mode, 2.52. This reduced n_{eff} is due to smaller size of the strip waveguides. The confinement of the strip waveguide is still high (0.78). In comparison to strip waveguide, the slot waveguide geometry has peak intensity in the low index slot, therefore, the TE_{neff} for slot waveguide is significantly smaller (1.76). T within silicon rails of the slot waveguide is also considerably reduced (0.45).

Table 2.1: Optical mode effective index (n_{eff}) and confinement (T) for different waveguide geometries illustrated in Fig. 2.2 and Fig. 2.3.

Waveguide	Effective Index(n_{eff})	Confinement(T)
Slab	2.86	0.82
Ridge	2.52	0.76
Strip	2.41	0.78
Slot	1.76	0.45

2.2.2 Single mode regime: strip waveguide analysis

Depending upon selected parameters optical waveguides can be single or multi-mode. For most applications single mode regime is preferred due to difficulty in coupling light selectively to higher order modes and resulting excessive inter-modal cross-talk. Single mode condition can be satisfied by varying geometric or material parameters of the waveguide. To study the effect of waveguide dimensions to mode properties, we consider a 220 nm high strip waveguide with varying width. The strip waveguide is embedded in the centre of a 2 μm X 2 μm area of SiO_2 material. Material index of Si (3.5) and SiO_2 (1.45) are unchanged. FMM mode solver is used for simulations. Waveguide width is iterated in steps of 50 nm from 150 nm until the second quasi-TE mode is observed above cut-off (n_{eff}=1.45). This condition is preserved until w=550 nm. For this range of widths, variation in n_{eff} and T is plotted in Fig. 2.4.

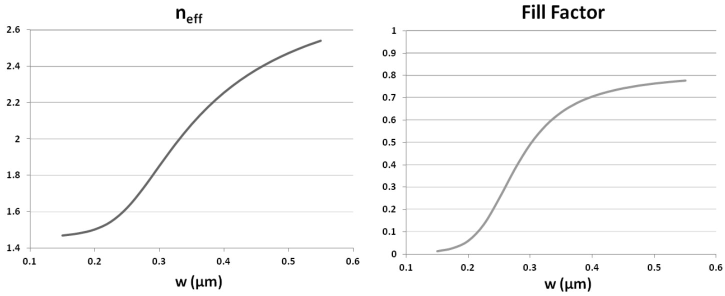

Figure 2.4: Variation of n_{eff} and T with width within the single mode regime of silicon strip waveguide of height 220 nm.

For w=150 nm, quasi-TE mode n_{eff} is 1.46 and T is 0.01. This is a weakly guiding mode with majority of the mode intensity outside silicon strip waveguide. Such a waveguide has a high probability to couple out of the waveguide through small-bends, substrate leakage or scattering of light [19]. However, as the width of the waveguide increases, both n_{eff} and T increase until T almost saturates to a value between 0.7-0.8. For example, the waveguide width of 450 nm has n_{eff} of 2.38 and T of 0.74. This clearly shows high confinement of the waveguide mode within the silicon core. Similarly increasing the height of the waveguide or material index contrast between core-cladding would also increase the n_{eff} and T within the single mode regime.

2.2.3 Optical loss in waveguides

Although bulk silicon is transparent to infrared light, losses in silicon based waveguides are non-negligible. One of the main reasons for losses within silicon waveguides is the scattering due to sidewall roughness. To increase light confinement in the waveguide it is typical to etch the slab vertically by dry-etch (such as by reactive ion etching (RIE)) or wet-etch processes to obtain strip or ridge waveguides Fig. 2.2 and Fig. 2.3. Although such processing is essential to obtain sufficient index-contrast for high confinement of light, it is a significant contributor to optical loss due to residual nanometric roughness on the etched vertical sidewalls. Another important contributor to loss is substrate leakage of optical mode. Further, it is also possible that light is absorbed by impurities in silicon or through surface absorption.

It is evident from Fig. 2.3 that the optical mode size reduces from ridge waveguide to strip waveguide. The vertical etch step creates nanometer-scale roughness on the sidewalls of the waveguide. Such roughness, even in nanometer regime, can contribute to losses as high as 10-20 dB/cm for silicon waveguides [20]. For strip/ridge waveguides scattering induced losses are often the most dominant contributor to optical mode propagation loss. Optical mode in a ridge waveguide experiences less scattering due to a shallow etch close to the core of the waveguide compared to deep etch in a strip waveguide. In the case of slot waveguide, the guided optical mode overlaps significantly with the etched vertical side walls of the slot region. Impact of sidewall roughness can be reduced by improving the etch recipe to minimize the resultant sidewall roughness. However, this can often be the most difficult approach due to limitations of the lithography process. The effect of the surface roughness on the scattering loss in dielectric waveguides has been theoretically studied and formulated [21]. The formula is represented by a function characterized by root mean square (RMS) roughness σ and the correlation length of the surface roughness l_c; the upper bound of the scattering loss α_{max}, as given in [21], is shown below.

$$\alpha_{max} = \frac{\sigma^2 \kappa}{k_0 d^4 n_1} \tag{2.14}$$

where, k_0 is wavevector of the light in vacuum, d, the half-width of the core, and n_1 represents the effective index of a silicon slab with the same thickness as the core. The factor κ depends on the waveguide geometry and the statistical distribution (Gaussian, exponential, etc.) of the roughness, in which the correlation length l_c is included. According to [22], κ is on the order of unity for most practical waveguide geometries. Thus, scattering loss is inversely proportional to d^4. In other words, it will increase in photonic wire waveguides with an ultra-small core. A roughness of only 5 nm, for instance, would cause a 60 dB/cm scattering loss in a 400 nm-wide core made of a 200 nm-thick silicon slab whose n_{eff} is 2.7. To achieve a practical scattering loss of a few decibels per centimetre, the surface roughness should be about 1 nm or less [23]. While there may also be others, there are two pertinent methods to reduce the impact of sidewall roughness:

- Post-processing

A commonly used method is to use post processing by covering the waveguides with silica (SiO_2). This reduces the refractive index contrast between silicon sidewall and cladding material interface. Surface trimming such as thermal oxidation of a thin top layer of silicon, or, laser ablation of the top surface of silicon, are other post-processing methods used for reducing the roughness on the surface of the waveguide [24], [25].

- Device design

It is also possible to reduce impact of surface roughness by selecting ridge waveguide geometry thereby reducing the vertically etched surface area. In a different approach, it is also possible to increase the size of the waveguide (for e.g. larger width) so the optical mode is highly confined within the waveguide and does not overlap significantly with the etched sidewalls [26]. Adiabatic tapering-out of strip waveguides is commonly used in straight sections to improve the performance of complex silicon photonic devices and circuits. Furthermore, Rayleigh scattering is inversely proportional to fourth order of wavelength. Therefore, shorter wavelengths are more impacted by sidewall roughness induced scattering than longer wavelengths.

Other loss mechanisms

- Substrate leakage

Careful choice of low-index substrate thickness is necessary to avoid light couple into the high index substrate. To avoid this problem, buffer layer such as buried oxide in SOI wafers of 2-3 μm thickness can be used to isolate the light guiding top surface (220 nm c-Si) of the wafer [27].

- Surface absorption

Si surface is susceptible to acquiring dangling *-OH* bonds. These *-OH* molecules have absorption tail extending into the 1.55 μm wavelength regime. Therefore in silicon photonics circuits operating at 1.55 μm wavelength *-OH* bonds on the surface may contribute to absorption of light [20].

- Impurities

During fabrication contamination such as metal impurities may be embedded in the SiO_2 cladding or Si core during fabrication. These impurities may contribute to scattering and absorption of the guided optical mode within the waveguide [28].

2.2.4 Dispersion

Dispersion is the temporal spread of light pulse or wave packet as it propagates through a material medium. Consequently it is dependent upon material index; which is itself a function of wavelength n(λ). This is known as material dispersion D_m. For bulk material systems D_m is the only contributor to total dispersion. However, for high confinement waveguides, the waveguide geometry strongly effects the dispersion of effective index, yielding waveguide dispersion, D_w. Total dispersion, $\boldsymbol{D}$, is then a sum of D_m and D_w. Group index n_g of a waveguide is related to its n_{eff} as shown in Eqn. 2.15. Further, dispersion equation is shown below (Eqn. 2.16).

$$n_g = n_{eff} - \lambda \frac{\partial n_{eff}}{\partial \lambda} \tag{2.15}$$

$$D = \frac{1}{c} \frac{\partial n_g}{\partial \lambda} \tag{2.16}$$

As discussed in [29] n_g and D significantly depend upon the mode field distributions within a strip waveguide. Since the mode field distributions of a quasi-TE and quasi-TM mode are different we observe different nature of n_g variation in the Fig. 2.5 below.

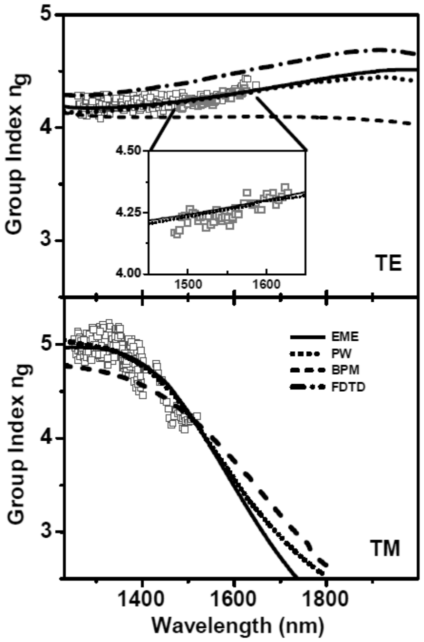

Figure 2.5: Group indices derived from transmission spectra in TE and TM polarization. Strip waveguide width is 525 nm and height 226 nm. Red and blue dots indicate measurements applying laser diodes and broadband LED light source respectively. *Source:[29].*

The simulations methods considered in the Fig. 2.5 are plane wave method (PW), eigenmode expansion (EME), beam propagation method (BPM) and finite difference time domain method (FDTD).

2.2.5 Birefringence

Birefringence is the property of a light guiding medium of anisotropic refractive index distribution. Due to the anisotropicity of refractive index, light experiences different propagation constants along the two orthogonal axes. This leads to phase differences between the two orthogonal modes. Single mode optical fibers for example have typically non-birefringent structure due to radial material symmetry. However, planar optical waveguides are generally strongly polarization sensitive i.e. strongly birefringent. It is important to note that in bulk optics *birefringence* is the optical property of a material having refractive index dependent upon polarization and direction of the propagating light. In this thesis the birefringence specifically refers to modal birefringence of the planar waveguide. The polarization-holding capacity of an optical waveguide is measured in terms of its beat length l_b, which is defined by

$$L_b = \frac{2\pi}{\beta_x - \beta_y} = \frac{\lambda}{\Delta n_{eff}}. \tag{2.17}$$

Achieving a non-birefringent geometry is non-trivial. Among the waveguides illustrated in Fig. 2.2 and Fig. 2.3 slot waveguide is usually the most and ridge waveguide can be least birefringent.

For applications such as telecommunications it may be essential to achieve non-birefringent integrated optical circuits. For such applications the polarization diversity approach is often utilized. In implementing such approach photonic circuit is designed for single polarization. Butt-coupling, polarization splitter and rotator can be used to realize a polarization diversity scheme schematically illustrated in Fig. 2.6.

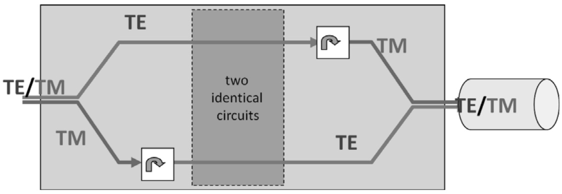

Figure 2.6: Schematic representation of a edge coupling based polarization diversity approach in a strongly polarization dependent 220 nm SOI platform. *Source: ePIXfab silicon photonics tutorial, University of Gent.*

Alternatively, as shown in Fig. 2.7 incoming randomly polarized light from the single mode optical fiber can be split into two orthogonal channels through a 2D polarization splitting grating coupler. The two orthogonal beams propagate through identical circuits. Finally, the two identical polarizations are recombined orthogonally through a 2D grating and coupled back onto a single mode optical fiber. Specifically for slot waveguides directional coupler based approach to handle different polarization states has also been proposed [30].

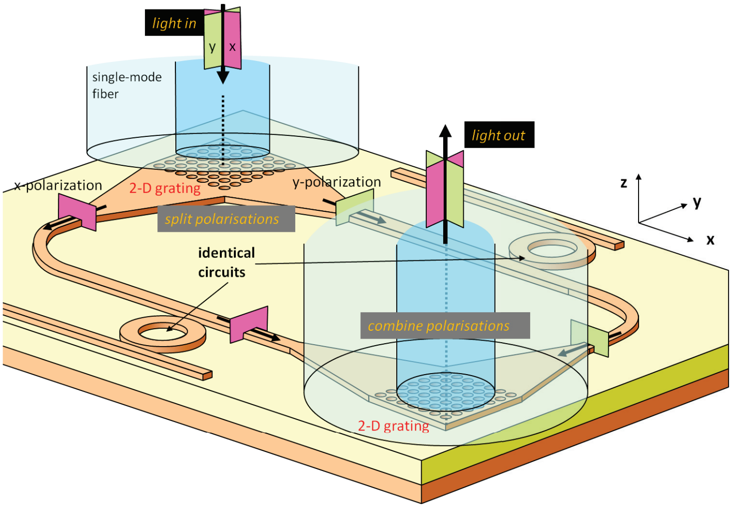

Figure 2.7: Schematic representation of a 2D grating assisted polarization diversity approach in a strongly polarization dependent 220 nm SOI platform. *Source: ePIXfab silicon photonics tutorial, University of Gent*.

3 Devices

3.1 Polarization issues

Capacity to handle arbitrary polarization states is important for waveguide devices, specially for telecommunication applications where single mode fibers are used. Therefore, integrated optic waveguides and circuits which can interface with single mode fibers seamlessly accepting the random polarization states are useful. If the waveguide material is used to achieve gain, it is important to have high confinement in the waveguide for both TE and TM polarization modes, to produce equal gain. However, when an optical gain device is operating in the saturated regime, there can be polarization-dependent gain, especially if the overlap of the modes at TE and TM polarizations is not high. To use optical non-linearities, it is also important to have high overlap between the two polarization modes in the region of the non-linear material, as otherwise the intensity distribution of the optical field, and thus the magnitude of the optical non-linear effect, would depend on the state of polarization. In Publication I and Publication II, multiple waveguide geometries, which guide both quasi-TE and quasi-TM mode within the single mode regime with varying degrees of overlap, are proposed.

3.1.1 Cross-slot waveguide

Cross-slot waveguide is proposed in Publication I. The cross-slot waveguide is schematically shown in Fig. 3.1. The device was first reported in [31]. However, in [31] it was shown that non-birefringence geometry cannot be easily realized. In Publication I we show that non-birefringence can be achieved in cross-slot waveguide, and, non-birefringent state may be attained by actively tuning the device through thermo-optic tuning. Fig. 3.1 shows typical geometric and material parameters used for the cross-slot waveguide simulations such as rail width, w_r, rail height, h, vertical slot width at the center of the slot, w_s, vertical slot base width, w_b ($w_b = w_s$ for perfectly vertical slot), horizontal slot height, h_s, depth of the horizontal slot, d, and thickness of the cover material, c, along with the refractive indices of different material layers. If $n_h = n_v$, the cross-slot configuration is called 'uniform', whereas when $n_h \neq n_v$ it is 'non-uniform'. We use refractive index of the substrate, n_{SiO2} as 1.46 and rails, n_{Si} as 3.58 for all simulations. In a cross-slot device it is possible to achieve non-birefringent structure through design of the waveguide cross-section geometry or post-processing by selecting appropriate atomic layer deposition (ALD) cladding material (n_v), and/or its thickness c. In Fig. 3.2 equal n_{eff} for quasi-TE and TM modes, shown by arrow, are observed for both uniform ($n_h = n_v = n_{SiO2} = 1.46$) and non-uniform ($n_h = n_{SiO2} = 1.46$ and $n_v = 1.63$) configurations, when vertical slot width, w_s=120 nm and d is centred ($d = (h - h_s)/2$). For simulation of the uniform structure we have used w_r=200 nm and $h = 400\ nm$ and for non-uniform structure, w_r=160 nm and $h = 380\ nm$. A similar study showing the design of non-birefringent cross-slot waveguide with angled sidewalls is also shown in Publication I.

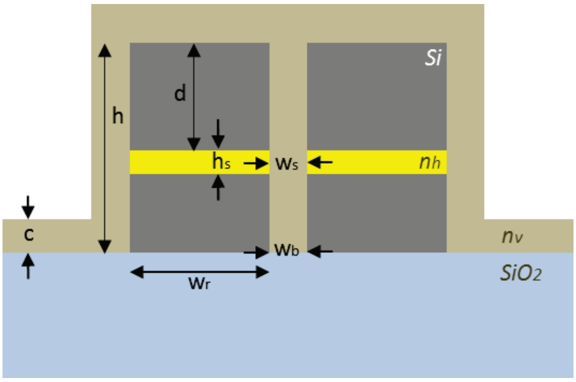

Figure 3.1: Schematic of a cross-slot waveguide.

The cross-slot waveguide also lends itself to polarization diversity, i.e., spatial localization of the quasi TE and TM modes. Therefore, the mode properties can be tailored, as an example, variation of T with depth of the horizontal slot is shown in Fig. 3.3 (a). It is shown that it is possible to achieve equal T of the two modes in the spatially localized horizontal and vertical slot regions. Equal confinement is obtained for d $\simeq$220 nm, which is close to the vertically centered horizontal slot waveguide. Parameters used for simulation are w_r=160 nm, h=450 nm, w_s=100 nm, w_b=60 nm, h_s=80 nm, c=100 nm and $n_h = n_v = 1.46$. The above example shows the possibility to change the mode characteristics in the design stage, or later, through post-processing.

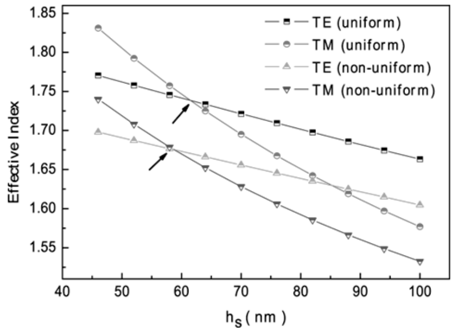

Figure 3.2: Equal n_{eff} for quasi-TE and TM modes, shown by arrow, are observed for both uniform ($n_h = n_v = n_{SiO2} = 1.46$) and non-uniform ($n_h = n_{SiO2}$=1.46 and n_v=1.63) configurations.

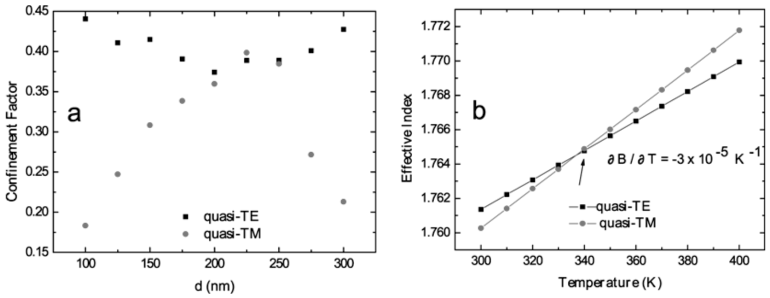

Figure 3.3: (a) T of the quasi-TE/TM modes with variation of depth in cross-slot waveguide is shown, and (b) variation of n_{eff} of quasi-TE and TM modes with temperature (T) for angled-wall cross-slot waveguide.

In Fig. 3.3(b), possibility to tune birefringence actively by thermo-optic means to realize zero birefringence is also shown. Importantly, during simulations we have assumed same temperature variation for the cross slot waveguide, therefore, both quasi-TE and TM modes are assumed to be influenced by a single heater source, unlike independent tuning of optical modes in typical polarization diversity schemes. Parameters used in simulation for Fig. 3.3(b) are, $w_r = 160$ nm, $h = 380$ nm, $w_s = 100$ nm, $w_b = 60$ nm, $h_s = 100$ nm, $d = 41$ nm, $c = 100$ nm and $n_h = n_{SiO2} = 1.46, n_v = 1.63$ and $\frac{\partial n_{SiO2}}{\partial T} = \frac{\partial n_h}{\partial T} = \frac{\partial n_v}{\partial T} = 10^{-5}$ K^{-1} at T=298 K.

Recently, cross-slot waveguide based directional coupler in III-V material system has been shown by Xiaoguang et al. [32].

3.2 Non-reciprocal devices

Realizing optical isolator and circulator functions is one of the remaining key challenges in silicon photonics[33]. Typically, such devices are based on non-reciprocal magneto-optic effects, and two main approaches use either, the Faraday rotation or, the non-reciprocal phase shift (NRPS) in waveguides [34]–[35]. Faraday rotation requires phase matching between TE- and TM-polarization modes, which is difficult to achieve. For this reason, there have been substantial efforts to utilize non-reciprocal phase change. The Faraday rotation can be considered as coupling between the two linear polarizations, but more fundamentally it is viewed as a difference in phase velocities between the two circular polarizations, induced by this magneto-optic coupling. NRPS is the change in the phase velocity of a linearly polarized guided wave from the same effect, and this change is in opposite directions for the two propagation directions in a waveguide. In Publication II we study the Faraday effect while in Publication III we utilize the NRPS to study non-reciprocal waveguides.

3.2.1 2D slot waveguide

To utilize Faraday rotation, multiple requirements have to be met. Non-birefringence is required to maintain the phase relationship between polarizations. Good optical mode overlap with magneto-optic material is needed for an efficient magneto-optic effect. High overlap between the two polarization modes is necessary for the magneto-optic effect to couple power efficiently between polarizations. Thus, there is strong interest in looking for waveguide configurations where both the quasi-TE and the quasi-TM modes are guided in the same region. To achieve strong light and magneto-optic matter interaction slot waveguide configuration while meeting the above requirements on polarization can be an asset. In order to simultaneously meet the multiple criteria we propose various slot waveguide geometries in Publication II. When appropriately designed, these 2D slot waveguide geometries allow zero birefringence and high overlap of the orthogonal polarizations. The studied geometries include closed 2D slot waveguide, open 2D slot waveguide (Fig. 3.4) and o-slot and u-slot waveguides (Fig. 3.5). O-slot concept is shown in Fig. 3.5 but due to its impractical shape it is excluded from simulation studies. The closed 2D slot, open 2D slot and u-slot waveguide geometries are compared for

n_{eff}, T and magneto-optic effect. In Eqn. 3.1, κ is the coupling of the two orthogonal polarization modes by Faraday rotation due to the magneto-optic slot material, θ_F is the Faraday rotation in the bulk material. Their ratio κ/θ_F is defined as the overlap coefficient between the polarization modes in the slot:

$$\kappa/\theta_F = \frac{2n_o\omega\varepsilon_o}{4k_o}\int\int_{slot} E^*_{TE,x}E_{TM,y}dxdy = \frac{n_o}{2Z_o}\int\int_{slot} E^*_{TE,x}E_{TM,y}dxdy. \tag{3.1}$$

Closed 2D Slot waveguide: In cross-section, 2D slot waveguide may be described as a super-position of horizontal and vertical slot waveguides with thin rails and wide slot regions. With increasing height h, n$_{eff}$ decreases for the quasi-TE mode but increases for the quasi-TM mode, and non-birefringence can be achieved by tuning the aspect ratio of the slot for w=300, 500 nm (Fig. 3.6). For w=300 nm, equal confinement for both polarization modes is reached at a value of h, higher than the non-birefringence height (Fig. 3.6b). Mode overlap κ/θ_F increases with h, as shown in Fig. 3.6(c).

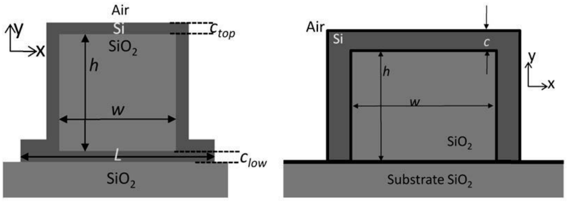

Figure 3.4: Schematic of a practical geometry for (a) closed 2D closed slot waveguide and (b) open slot waveguide.

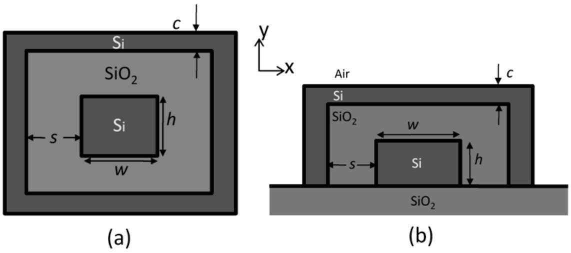

Figure 3.5: Schematic of (a) O-slot waveguide and (b) U-slot waveguide.

In Fig. 3.7, the variation with under-cladding thickness c_{low} is studied for w=300,500 nm geometries. For w=300 nm, with increase in c$_{low}$, the quasi-TE n$_{eff}$ increases, but the T in the slot first reaches a maximum value and then decreases. This is due to the larger overlap of the quasi-TE mode field with the thicker high-index under-cladding. However, the n_{eff} of the quasi-TM mode increases with a thicker c_{low} and the T in the slot region also increases as the mode field for the quasi-TM polarization is confined to the slot by the bottom and top parts of the frame. κ/θ_F for the polarization modes in the slot decreases with increasing c_{low} since the two modes are affected differently by this horizontal layer. For w=500 nm, less variation in under-clad thickness is allowed for single-mode operation. n_{eff} is not affected significantly, T in the slot is about twice as large as with w=300 nm, and κ/θ_F decreases with increasing c_{low}. Isotropic medium behavior (non-birefringence) or equal T is achieved for w=300 nm, but not for w=500 nm. The effect of varying overcladding thickness c_{top} with w=300,500 nm is studied in Fig. 3.8. With increasing c_{top}, n_{eff} values for both polarization modes increase. In the single-mode regime, the T values first reach a maximum and then decrease, except for the quasi-TE mode when w=500 nm, for which T increases monotonically with increasing c_{top}. The value of κ/θ_F increases for both w=h=300, 500 nm geometries with increasing c_{top}, and it is again much larger when w=500 nm. Zero birefringence is achieved with both slot sizes and equal T for w=500 nm. The results in Fig. 3.7 and Fig. 3.8 have significantly different characteristics since the top Si layer (c_{top}) is different from the bottom Si layer (c_{low}). Because of the overcladding deposition on the sidewalls of the slot, the overcladding provides the slot confinement effect for both polarizations. The simulation results demonstrate the flexibility offered to the designer in realizing closed 2D slot waveguide with custom mode properties. All geometries presented above do not suffer from extreme lithographic constraints. Further the sub-100 nm features such as c_{top} or c_{low} are realized through depositions steps which are often timed to obtain nanometric accuracy. In Publication II, a similar analysis for open-2D slot waveguide and u-slot waveguide shows that high mode overlap, confinement in the low index region and non-birefringence of the optical modes can be achieved with appropriate design or post processing.

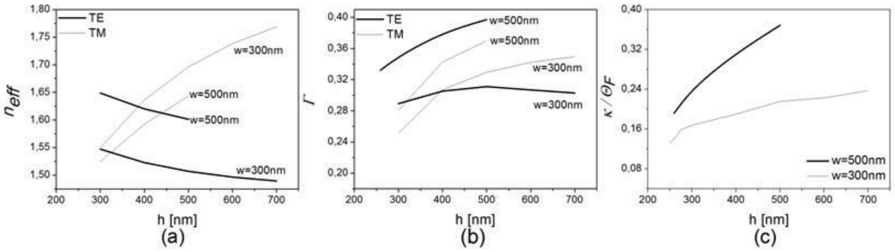

Figure 3.6: Variation in (a) n_{eff}, (b) T and (c) κ/θ_F for change in aspect ratio in a practical closed 2-D slot waveguide when w=300,500 nm, $c_{low} = 30\ nm$ and $c_{top} = 60\ nm$. L=600 nm for w=300 nm and L=800 nm for w=500 nm.

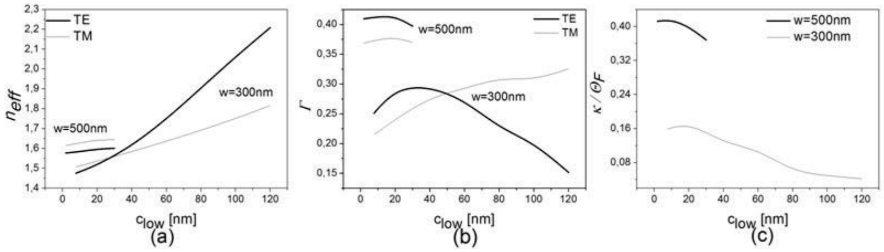

Figure 3.7: Variation in (a) n_{eff}, (b) T and (c) κ/θ_F for change in c_{low} in a practical closed 2-D slot waveguide when w=h=300, 500 nm and $c_{top} = 60\ nm$. L=600 nm for w=300 nm and L=800 nm for w=500 nm.

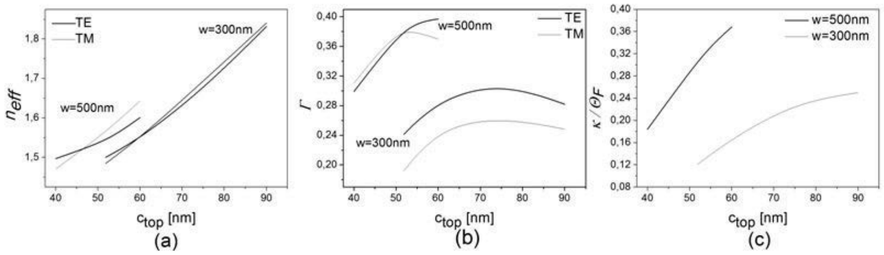

Figure 3.8: Variation in (a) n_{eff}, (b) T and (c) κ/θ_F for change in thickness of top-cladding c_{top} in a practical closed 2-D slot waveguide when w=h=300, 500 nm and $c_{low} = 30\ nm$. L=600 nm for w=300 nm and L=800 nm for w=500 nm

3.2.2 Asymmetric slot waveguide

Magneto-optic device based on Faraday rotation requires phase matching between polarizations which is non-trivial. Therefore there is also significant interest in single polarization NRPS based devices. A non-reciprocal isolator and circulator devices based on NRPS can be realized as Mach-Zehnder interferometers [36]. Some of the highest efficiencies achieved for NRPS have been published for silicon waveguides integrated with magneto-optic garnets [37], [38]. However, there still remain further challenges in integrating garnet materials with semiconductors [35, 39, 40]. In Publication III we present the results of modelling silicon slot waveguides with magneto-optic material filling the slot. Magneto-optic polymers [41] or polymer composite materials [42] are of particular interest, since they are promising for integration with slot waveguides and have shown high magneto-optic coefficients. NRPS properties of slot waveguides are studied using a model for a 1-dimensional, 5-layer slab waveguide, illustrated in Fig. 3.9. We limit our study to structures with the shown symmetry for refractive indices of materials, which is a typical case for vertical slot waveguides. The layer 3 is a slot filled with a magneto-optic material, having refractive index n_s and a thickness h_s. The layers 2 and 4 are high-index rails with refractive index n_r and thicknesses h_l and h_t, respectively. The waveguide is surrounded by a low-index material of the semi-infinite layers 1 and 5, with refractive index n_c. Optical wave propagation is in the direction of the z-axis, and interfaces between the slabs are normal to the x-axis. For the TM-polarization, the main electric field component of the guided wave is E_x, but a guided mode also has an axial component E_z. These two orthogonal components of the electric field have a phase difference of $\pi/2$, so at locations where neither of them is zero, there is elliptic polarization, in the plane of propagation. With an external magnetic field in the direction of the y-axis, normal to this plane of the electric field of the wave, magneto-optic effect causes coupling between the orthogonal components of the electric field of the wave, similar to the Faraday rotation. This causes a shift of the propagation constant. In a symmetric waveguide, elliptic polarizations at mirror-image locations are of opposite handedness, so the total magneto-optic phase shift cancels out to zero. Therefore, some asymmetry in the waveguide structure is required to generate the NRPS effect.

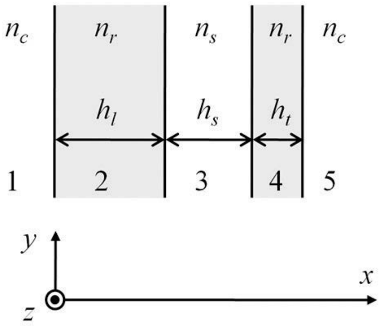

Figure 3.9: Asymmetric slot waveguide as a 5-layer slab structure.

The dielectric tensor for an isotropic magneto-optic slot material having refractive index n$_s$ is, with the selected direction for the magnetic field,

$$\begin{bmatrix} n_s^2 & 0 & -i\epsilon_{xz} \\ 0 & n_s^2 & 0 \\ i\epsilon_{xz} & 0 & n_s^2 \end{bmatrix} \tag{3.2}$$

Here, non-diagonal elements couple x- and z-components of the electric field, with $\epsilon_{xz} = 2ns\theta_F/k_0$, where θ_F is the specific Faraday rotation in the material, and κ_o= 2π/λ. The shift of propagation constants β_f and β_b, for forward and backward propagation, respectively, is given by a perturbation calculation Eqn. 3.3 as,

$$\Delta\beta = \beta_f - \beta_b = \omega\epsilon_o \int E^*(x)\Delta\epsilon E(x)dx \tag{3.3}$$

where, the dielectric perturbation tensor $\delta\epsilon$ has only the non-diagonal elements of Eqn. 3.2, and its diagonal elements have values of zero. The mode field distribution of unperturbed waveguide is normalized to unit power. For the TM mode,

$$\Delta\beta = 2i\omega\epsilon_o \int \epsilon_{xz}E_x(x)E_z(x)dx. \tag{3.4}$$

For a slab waveguide, the longitudinal field component can be expressed in terms of the transverse component,

$$E_z(x) = \frac{i}{\beta}\frac{dE_x(x)}{dx} \tag{3.5}$$

with propagation constant β of unperturbed waveguide. We get,

$$\Delta\beta = \frac{-2\omega\epsilon_o}{\beta} \int \epsilon_{xz}E_x(x)\frac{dE_x(x)}{dx}dx. \tag{3.6}$$

This can be integrated, inserting $\omega\epsilon/\beta = 1/(Z_o n_{eff})$, with Z_o, the impedance of free space and n$eff = \beta/k_0$, to give,

$$\Delta\beta = \sum_{j-1..5} \frac{-1}{Z_o n_{eff}}\epsilon_{xz}\left[E_x^2(x_j^+) - E_x^2(x_j^-)\right]. \tag{3.7}$$

The sum is over different layers, and it is including squares of the electric field amplitude inside the layer at the two interfaces, at the positions x_j^- and x_j^+. Unperturbed solutions giving the mode field distribution and the effective index n_{eff} were solved with a thin-film matrix method [43] for a 5-layer slab model. In modeling NRPS, we concentrate on the fundamental TM mode, and mainly look for structures guiding only the fundamental mode for the TM polarization. As ϵ_{xz} has a non-zero value only in the slot, there is only one term in the sum of Eqn. 3.7. All calculations are made for the wavelength $\lambda_o = 1.55\ \mu$m. For magneto-optic operation, the requirements for waveguide properties differ from those typically expected from slot waveguide structures. It is seen from Eqn. 3.7 that the goal is to maximize the change in normalized intensity across the slot layer. High NRPS is important for having short device lengths, but an important figure of merit is the ratio between values representing NRPS and waveguide loss [35],[40]. Magneto-optic material can contribute fundamental absorption, and the loss from this can be calculated as a product of the material bulk attenuation coefficient and the mode confinement factor in the magneto-optic material. The confinement factor T in the slot is calculated as [44],

$$\Gamma = \frac{n_s}{Z_o} \int_{x_3^-}^{x_3^+} \left|\overline{E}(x)\right|^2 dx. \tag{3.8}$$

For simulations, we use SiO_2 with n_c = 1.46 as the surrounding cladding material, and the slot layer refractive index was taken to be n_s = 1.50. The required asymmetry can then only be achieved by a difference of the rail widths, which can also be considered as an offset of the slot position from the waveguide center. As typically NRPS was observed to increase with increased asymmetry, we decided to have the width of $h_t = 50\ nm$ for the narrower rail, as a lower limit for a practical waveguide. This leaves two free parameters: the wider rail width h_l and the slot width h_s. Fig. 3.10 shows the $\delta\beta/(\epsilon_{xz})$ contours and the single-mode region boundary for this material combination. The achieved optimum $\delta\beta/(\epsilon_{xz})$ coefficient is at a high level (about $\delta\beta/(\epsilon_{xz})$ = 1.13 μm^{-1}). Interestingly, the confinement factor in the slot is T = 0.6 for such an optimal single mode waveguide, which is even lower than the value of T= 0.69 for the previously published magneto-optic waveguides with high NRPS [37, 38, 45].

For silicon waveguides both from [37, 38, 45] and in the examples given here, the values for $\delta\beta/(\epsilon_{xz})$ are at the same level, and this roughly represents the maximum achievable with slot or strip waveguides. With the presented asymmetric slot waveguides based device silicon photonics can take advantage of the high Verdet constant based magneto-optic polymeric nano-composites.

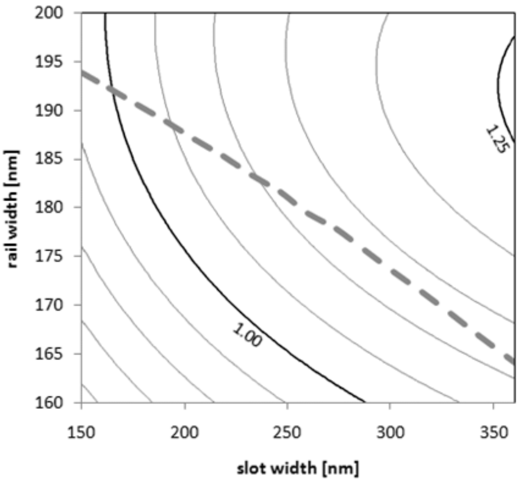

Figure 3.10: $\delta\beta/\epsilon_{xz}$ in μm^{-1} of an asymmetric 5-layer waveguide as a function of widths of the wider rail h_l and slot h_s. Here h_t=50 nm, and n_r=3.48, n_c=1.46, n_s=1.5. Contours are drawn for values of $\delta\beta/\epsilon_{xz}$=0.80, 0.85,..,1.25 in μm^{-1}, from bottom to top, respectively. Dashed line shows the boundary of single mode operation for quasi-TM modes.

3.3 Non-linear properties

The etching processes used in the manufacturing of silicon photonics typically result in angled sidewalls, which affects properties of the slot waveguide. The angled sidewalls provide improved accessibility from top, which has been proposed to be used in sensing applications [46]. Schematic of a angled sidewall slot waveguide is shown in Fig. 3.11.

In Publication IV we demonstrate complete filling of such a dry-etched angled-sidewall slot structure with TiO_2 grown by the ALD technique. Fig. 3.12(a) shows that the slots are completely filled. Titania (TiO_2) is one of the most common ALD grown materials, and it is also a promising candidate for an ALD grown nonlinear slot filling material. It has a refractive index of 2.2. Moreover, it has been reported to exhibit a very large nonlinear index n_2 for an oxide; it is about 50 times larger than n_2 of SiO_2 [47]. Using prism coupling measurements, optical loss of the ALD grown TiO_2 has been observed to be less than 1 dB/cm [48], which is several times smaller than the typical loss in the slot waveguide itself. In Fig. 3.12(b), the laminate consists of alternating 10 nm layers of Al_2O_3 and TiO_2. The refractive index of Al_2O_3 is 1.64; note that by varying the layer thicknesses, the Al_2O_3-TiO_2 laminate therefore enables range of refractive index between 1.64 and 2.2 [49]. Further, it has also been shown that the ALD nanolaminate may have potential to be used in the manufacture of highly nonlinear nanocomposites with excellent precision [50], [51].

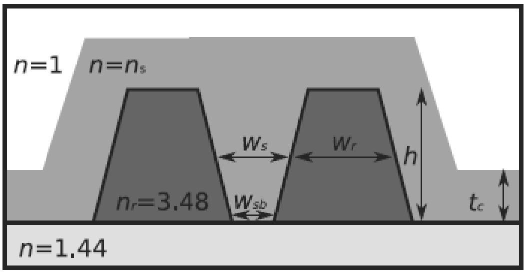

Figure 3.11: Schematic of thin film filled slot waveguide and introduction of its parameters.

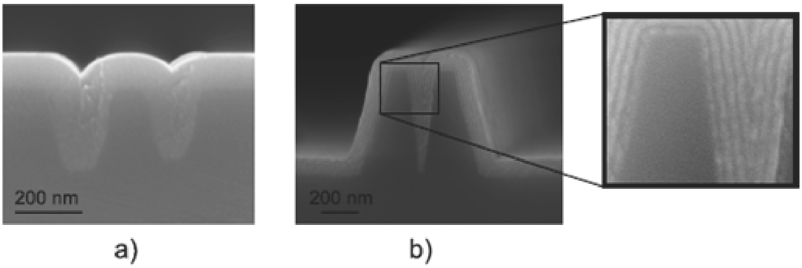

Figure 3.12: SEM of a cross section of slot waveguide test structures filled with a) ALD grown TiO_2, b) laminate of alternating layers of Al_2O_3 and TiO_2.

Angled sidewalls also affect the T properties of the waveguide, which has been briefly discussed in earlier studies [52],[53]. However, the comparisons have been made between slot waveguides with different cross sectional area, and it is therefore difficult to observe the fact that the angled sidewalls actually enhance the vertical confinement of the optical field [46], [54]. We also study the effect of the sidewall angle and filling material on the nonlinear properties of the waveguides. In order to evaluate the expected performance of real all-optical devices, non-linearities in each part of the waveguide need to be taken into account. The effective non-linearity of the mode is calculated as:

$$\gamma = \frac{n^2}{Z_o^2} \frac{\int |E(x,y)|^4 \cdot n_2(x,y) dA}{\left| \int Re\left\{E(x,y) \times H^*(x,y)\right\} \cdot u_z dA \right|}, \tag{3.9}$$

where u_z is a unit vector. This equation gives the n_{eff} change of the waveguide mode caused by the optical power in units 1/W. In silicon based all-optical devices, the non-linear loss parameter α_2 is of an essential importance. In order to determine a figure of merit (FOM) for the non-linear n_{eff} change against α_2 in the waveguide, ratio between the two is determined:

$$FOM_{n_2/\alpha_2} = \frac{\int |E(x,y)|^4 \cdot n_2(x,y) dA}{\int |E(x,y)|^4 \cdot \alpha_2(x,y) dA} \tag{3.10}$$

Note that even when the filling material is assumed to exhibit no nonlinear loss, some nonlinear loss exists in the waveguide, because a small fraction of the electric field resides in the silicon rails with a considerable nonlinear loss. The refractive index values and nonlinear parameters used in calculations are shown in Table 3.1. Fig. 3.13 shows the effective nonlinearity and FOM $n2/\alpha_2$ in TiO_2 filled slot waveguides as a function of w_{sb} and w_s. Note that for silicon, FOM_{n_2/α_2} = $1.42 \cdot 10^{-7}\ m$. It has also been plotted into Fig. 3.13 to give a reference for the performance of silicon waveguides. The effective nonlinearity is not much affected by the sidewall angle, indicating that the vertical mode compression is not very significant with TiO_2 (n = 2.2) as the cover material. The n_2/α_2 FOM decreases with increasing sidewall angle. The decrease of FOM_{n_2/α_2} indicates weakened mode confinement of the mode into the slot, with a larger fraction of the optical field in silicon, the mode experiences a higher nonlinear loss. Despite being highly nonlinear for an oxide, TiO_2 still has a lower nonlinearity than silicon. Therefore, materials with higher nonlinearity would be desired to realize extremely nonlinear slot waveguide. Even though excellent nonlinear properties have been demonstrated with polymer-clad silicon slot waveguides, inorganic materials have benefits over polymers in terms of manufacturability and environmental stability. One example of an inorganic highly nonlinear material is silicon nanocrystals, which are reported to have nonlinearity of nearly 100 times larger than TiO_2. The refractive index of such a material system can be as low as 1.55 [55], [56]. Therefore, angled sidewalls have advantages with this material system, as seen in Fig. 3.14. The effective nonlinearity for Si nanocrystal filled slot waveguides is about 50 times larger than with TiO_2, and it increases significantly with angled sidewalls. Note that the n_2/α_2 FOM for silicon nanocrystals is $8 \cdot 10^{-7}$ m, and for silicon it is $1.42 \cdot 10^{-7}$ m. The α_2 of silicon nanocrystal filled silicon slot waveguides is therefore limited by FOM_{n_2/α_2} of silicon nanocrystals. It can be seen that with nearly vertical sidewalls, FOM_{n_2/α_2} of silicon nanocrystal filled slot waveguides is very close to that of silicon nanocrystal material, indicating strong optical confinement into the slot. FOM_{n_2/α_2} decreases slightly when $w_{sb} = 0$, due to a larger fraction of the field in the silicon rails when w_{sb} is small. Alumina (Al_2O_3) is one of the most common ALD materials. It is also a very common material for Erbium doped waveguide amplifiers [57]. ALD has been proven to be suitable for growing materials with well-controlled doping [58] therefore, ALD filled slot waveguides are potential candidate if silicon based emitters for telecommunication wavelengths are considered. The modal gain in a high-index-contrast waveguide can be calculated using the confinement factor T, which gives the ratio of the modal gain in the waveguide to the bulk gain of the filling material [59].

Table 3.1: Material parameters used in the calculations, and the wavelengths for the given parameters.

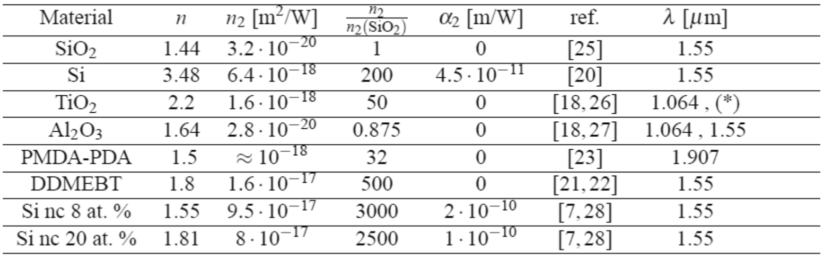

Material	n	n_2 [m^2/W]	$\frac{n_2}{n_2(SiO_2)}$	α_2 [m/W]	ref.	λ [μm]
SiO_2	1.44	$3.2 \cdot 10^{-20}$	1	0	[25]	1.55
Si	3.48	$6.4 \cdot 10^{-18}$	200	$4.5 \cdot 10^{-11}$	[20]	1.55
TiO_2	2.2	$1.6 \cdot 10^{-18}$	50	0	[18,26]	1.064 , (*)
Al_2O_3	1.64	$2.8 \cdot 10^{-20}$	0.875	0	[18,27]	1.064 , 1.55
PMDA-PDA	1.5	$\approx 10^{-18}$	32	0	[23]	1.907
DDMEBT	1.8	$1.6 \cdot 10^{-17}$	500	0	[21,22]	1.55
Si nc 8 at. %	1.55	$9.5 \cdot 10^{-17}$	3000	$2 \cdot 10^{-10}$	[7,28]	1.55
Si nc 20 at. %	1.81	$8 \cdot 10^{-17}$	2500	$1 \cdot 10^{-10}$	[7,28]	1.55

$$\Gamma = \frac{n_A c \epsilon_o \int |E(x,y)|^2 \, dA}{\int Re\{E(x,y) \times H^*(x,y)\} \cdot u_z dA} \tag{3.11}$$

Sidewall angles typical of RIE can have an enhancing effect on the effective area and nonlinearity of mode in slot waveguides. On the other hand, with larger sidewall angles, a larger fraction of optical power resides in the silicon rails, increasing nonlinear loss. Therefore, for optimum slot waveguide structure, proper balance between these effects needs to be found, depending on the used nonlinear slot material.

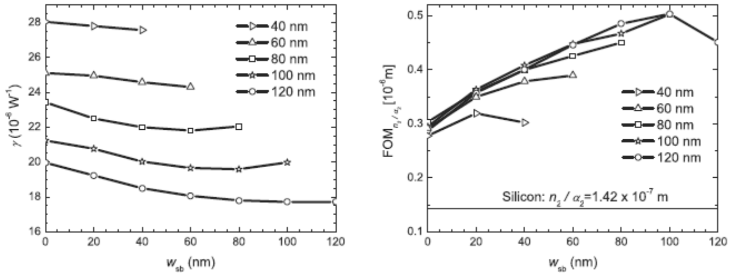

Figure 3.13: Effective nonlinearity and n_2/α_2 figure of merit in TiO_2 filled slot waveguides with w_r=160 nm and h=260 nm, as a function of w_{sb} at different w_s from 40 nm to 120 nm.

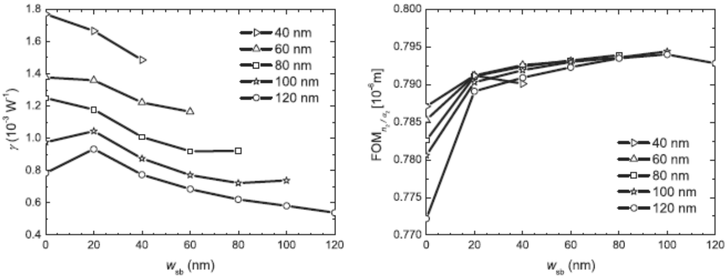

Figure 3.14: Effective nonlinearity and FOM_{n2/α_2} in silicon nanocrystal filled slot waveguides with w_r=160 nm and h=260 nm, as a function of w_{sb} at different w_s from 40 nm to 120 nm

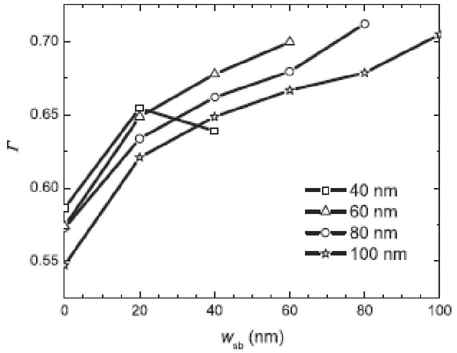

Figure 3.15: Confinement factor for gain in Al_2O_3 filled slot waveguides with w_r=160 nm and h=260 nm, as a function of w_{sb} at different w_s from 40 nm to 100 nm.

3.4 Low loss

Nanometric smooth sidewalls and surfaces for low-loss photonic wires are not mandatory for traditional digital CMOS industry, therefore achieving very low loss waveguides on a CMOS platform poses a challenge for CMOS nanophotonics. Our study so far has focussed on the 1.55 μm wavelength using silicon as the guiding material. CMOS technology also lends SiN as a choice for photonic wire material. Previously, SiN based devices have been demonstrated using strip and ridge waveguides, and the SiON based 'A-shaped' box waveguide [60, 61, 62, 63, 64]. Enabled by the broad spectrum transparency, moderately high refractive index (2.0) and low-loss, Si_3N_4 based integrated optics is gaining prominence in diverse domains ranging from telecom to life sciences [65, 66, 67, 68, 69]. Together, these factors have contributed to interest towards developing a Si_3N_4 photonic platform for the visible and very near infrared (VNIR) wavelength regime (400-1000 nm) [70],[71]. However, the path to a mature Si_3N_4 technology on the CMOS infrastructure requires foremost, the realization of passive optical devices with low-losses.

In Publication V, a method to reduce surface roughness of the Si_3N_4 photonic wire waveguide manufactured on a 200 mm CMOS pilot-line is investigated. Non-optimized processing resulted in nanometer-scale surface roughness and consequently high propagation loss. Over such a high loss device, 40 nm Al_2O_3 is deposited by ALD technique. Si_3N_4 strip waveguides possesses much lower material index contrast but nevertheless, at shorter wavelengths (visible-VNIR), sidewall roughness remains the major source of the waveguide loss because of the Rayleigh scattering, which is inversely proportional to the fourth power of the λ. Therefore, the influence of scattering on the propagation loss is expected to be more pronounced in Si_3N_4 material system at visible-VNIR wavelengths vis-á-vis silicon photonics in the infrared regime[1]. In Publication V we have studied the influence of ALD deposition of a thin layer of Al_2O_3 on the surface roughness and loss in a 220 nm x 500 nm Si_3N_4 based wire waveguide.

---

[1] Refer [19], [72] for use of ALD layers to reduce waveguide propagation loss in the infrared wavelength regime.

3.4.1 Fabrication

A 200 mm bare Si wafer is used as the substrate. Firstly, plasma enhanced chemical vapor deposition (PECVD) is used to deposit 2.4 μm SiO_2 followed by 220 nm thick Si_3N_4 layer. The silane, nitrogen and ammonia gas flows are optimized for Si_3N_4 deposition at 400 C, which ensured CMOS back-end compatibility. After the layer deposition, the waveguide and the grating coupler (GC) are patterned by using 193 nm optical lithography and RIE process. The waveguide is deeply etched (220 nm deep), and the GCs are defined with different etch-depths by controlling the etch duration. Photo-resist is used as an etch mask for both the etch processes. After dry etching, the wafers are cleaned by using oxygen plasma and a wet chemical process. The widths of the waveguides are in the range of 500+/-30 nm. After dicing, an Al_2O_3 film is deposited over a batch of Si_3N_4 chips by ALD process. In this ALD process a 40 nm film of Al_2O_3 is grown at 120 C by using tri-methyl aluminum (TMA) and H_2O as precursors with ALD TFS 200 equipment by Beneq. At the same time a silicon dummy sample is coated in the same chamber and it is used for characterization of the ALD grown film. After fabrication the cross-section SEM micrograph of the Si_3N_4 wire is shown in Fig. 3.16.

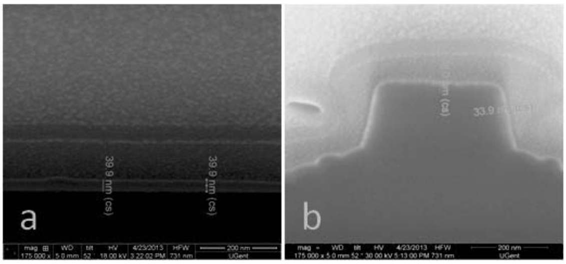

Figure 3.16: SEM micrographs of the 40 nm Al_2O_3 ALD clad Si_3N_4 waveguide cross-sections prepared using FIB milling. (a): SEM cross section image of the dummy sample placed in the chamber during ALD deposition, measured thickness of deposited Al_2O_3 is 39.9 nm. (b) Lower contrast SEM image of deposited Al_2O_3 over the Si_3N_4 waveguide.

3.4.2 Experiment

The refractive index of 220 nm Si_3N_4 and 40 nm Al_2O_3 are determined using ellipsometry before and after ALD deposition, respectively. The roughness of the waveguide surface is compared prior-to and after 40 nm Al_2O_3 deposition using atomic force microscopy (AFM). The propagation loss in the 500 nm wide wire is compared by cut-back method using spiral waveguides of different lengths (1, 2, 4 and 7 cm). These measurements are performed for the TE polarization using a tunable laser source emitting in the range 890–910 nm and a single mode fibre at this wavelength range. The GC measurements are performed by coupling unpolarized light from a tungsten halogen white light source (400 nm –1700 nm) using a single mode fibre into the waveguides. Another similar fibre is positioned above the output GC to collect the light into an optical spectrum analyzer. The coupling efficiency is determined from the fibre-to-fibre transmission. The position of the fibre is optimized for maximum transmission.

3.4.3 Results

After fabrication air clad dies were characterized for roughness. RMS surface roughness of 1.73 nm and peak roughness of 9 nm was measured by AFM. Compared with previously reported loss versus roughness data in [73] this is very high roughness level. However, after 40 nm Al_2O_3 coating RMS roughness of 0.42 nm and peak roughness of $\simeq$2 nm was measured by AFM. Cut-back measurements prior to ALD coating were indeterminable due to very high excess loss. After ALD coating cut-back measurements are performed and results are show in Fig. 3.17

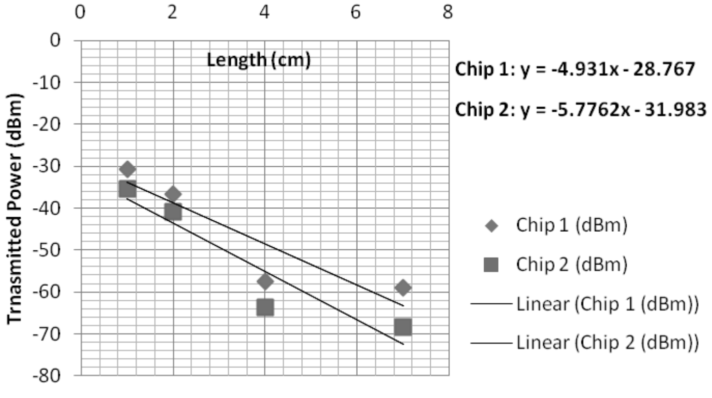

Figure 3.17: Graph shows cut-back measurement results after 40 nm ALD deposition of Al_2O_3. Chip1 and Chip2 exhibit much reduced loss of 4.9 dB/cm and 5.8 dB/cm, respectively.

Firstly, both the dies show much reduced excess loss which enabled the cut-back measurement. Secondly, the measurements are performed well above the noise floor of the detector thereby making the cut-back measurements reliable. Chip1 exhibited a waveguide loss of 4.9 dB/cm whereas Chip2 showed a loss of 5.7 dB/cm. As with surface roughness results, the ALD Al_2O_3 coated Si_3N_4 waveguides show loss values similar to previously reported Si_3N_4 waveguides in [73]. In order to ascertain the origin of $\simeq$30 dB excess loss in the cut-back method results, white light measurements are used to characterize the grating couplers. The results show that the loss due to GCs at 900 nm wavelength is 20 dB (10 dB per GC). The remaining 10 dB loss is attributed to the bends in the spiralling waveguides which have a bend radius of 10 μm. For Si_3N_4 waveguides the minimum bend radius for almost lossless transmission is estimated to be 25 μm. Optical images of the Si_3N_4 chips prior-to and after ALD coating of 40 nm Al_2O_3 film are obtained using a CMOS camera. Images shown in Fig. 3.18 are obtained at the same magnification settings of the microscope and similar ambient brightness, thus reducing the variations due to the camera set-up and environment. Care was taken not to saturate the camera by working at lower power. A comparison of these images clearly indicates the reduction in the light scattering from the waveguides after ALD deposition. By measuring the decay in the light intensity along the length of the waveguide it is possible to estimate the waveguide loss due to scattering before and after ALD coating. The experiment indicates extremely high loss prior-to ALD coating ($\simeq$60 dB/cm) whereas the loss after ALD coating was 5-6 dB/cm, which re-confirms the loss measured by the cut back method (Fig. 3.17). In Fig. 3.18(b) the slope appears to be positive. This anomaly is attributed to the scattering due to contamination at the edge of the acquired image. Publication V demonstrated a CMOS compatible post-processing methodology to reduce propagation loss in 500 nm x 200 nm wire from very high to low-loss regime. Such a methodology can also be used to tune the spectral performance of critically coupled devices such as ring resonators while simultaneously improving the overall performance of the passive circuits through reduction of surface roughness.

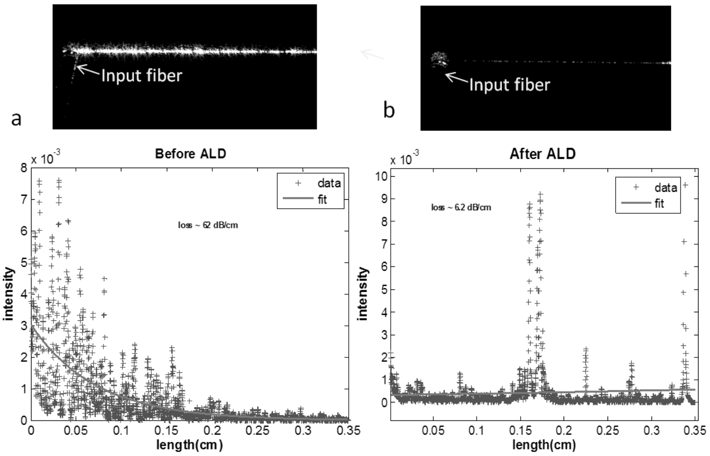

Figure 3.18: Image captured through an optical microscope of Si_3N_4 wire conducting light coupled through a GC. (a) Air clad ALD waveguide (b) 40 nm Al_2O_3 ALD coated Si_3N_4 wire.

4 Summary and Outlook

4.1 Summary and future work

In this section previously discussed results are used as background to propose a path forward for future investigations.

2D-slot waveguide demonstration

Thus far polarization overlap enabling 2D slot waveguides cross-sections studied in Publication II, have not been demonstrated. However, box-shaped waveguide [68], a similar geometry to the closed-2D slot waveguide, has been demonstrated in the SiON material system. On this platform, losses as low as 0.1 dB/cm have been shown. Such low loss is in-part possible due to lower refractive index contrast in the SiON material system. Since propagation loss in slot waveguide is strongly dependent upon side wall roughness and index contrast, losses in SOI material system are expected to be higher. Nevertheless, practical demonstration of the 2D slot waveguide geometries is an important next step. Furthermore, although we have studied the issue of on chip polarization control, initial coupling of light into these non-birefringent waveguides is still to be investigated.

On-chip Faraday rotation device

We have investigated in Publication II open 2D slot waveguides which can be suitable devices for magneto-optic material integration. Separately, in University of Arizona's College of Optical Sciences, magneto-optic polymers with magnetite nanoparticles embedded in a PMMA matrix have been studied to realize magneto-optic nanocomposite. To demonstrate a Faraday rotation device, an inverted open 2D slot waveguide can be used, as shown in Fig. 4.1. The motivation to study such devices is to utilize tailored highly magneto-optic nanocomposites and efficient integrated photonic design to enable high optical mode field overlap with the magneto-optic nanocomposite material. Such a device can be realized starting with an oxidized silicon wafer followed by optical lithography to fabricate etched groove for inverted 2D slot in SiO_2. Finally, ALD or PECVD grown high index material can be used to realize the rails. Such an inverted open-2D-slot geometry can be integrated with spin coated magneto-optic polymer as the final step. Intensity field of an inverted 2D slot is simulated with the FMM solver and shown in Fig. 4.2. Waveguide groove width of 450 nm, waveguide depth of 220 nm and high index rail of 40nm is used for simulations. Silicon (n=3.5) is assumed as the rail material, and silica (n=1.46) as slot cladding material. PMMA (n=1.5) is assumed to fill the slot. The quasi-TE mode n_{eff} of 1.57 and T of 0.12 is obtained.

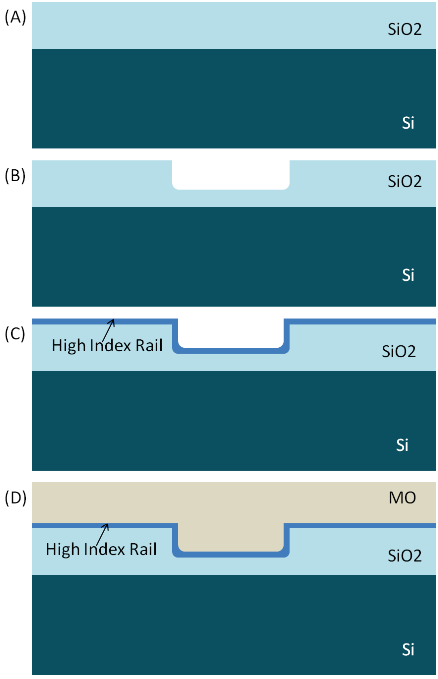

Figure 4.1: Step-wise schematic of the 2D waveguide fabrication process to realize a Faraday rotation device with spin coated MO polymer membrane on top.

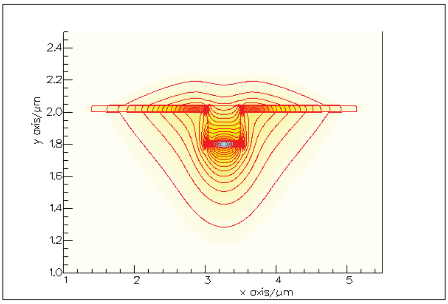

Figure 4.2: Intensity plot of the quasi-TE mode in inverted 2D slot waveguide.

Very low loss waveguides

In Publication V we demonstrate that loss in Si_3N_4 integrated optical platform can be significantly reduced with thin-film ALD layers. Such layers not only reduce surface roughness, but also reduce the refractive index contrast at the surface of silicon or Si_3N_4 based waveguides. Although we demonstrated that loss can be reduced from very high (>60 dB/cm) to 4-5 dB/cm for Si_3N_4 based 500 nm strip waveguides at 980 nm wavelength, it may also be possible to reduce loss from ’low’ to ’very-low’ regime (<0.5 dB). Varying ALD laminate composition on top of the strip waveguides of silicon or Si_3N_4 can be used to obtain a Gaussian index profile; similar to graded index fibers. For fundamental quasi-TE modes, such deposited layers will be symmetric, thereby preserving the polarization state, and significantly reducing residual nanometric surface roughness after processing. ALD based laminates of Al_2O_3 and TiO_2 may be used to realize meta-material characteristics by tailoring the composition of the laminate to obtain gradually varying index to match cladding and core refractive indices with suitable index gradients.

Throughout the study, care was taken to ensure practical geometries are investigated. The presented studies provide the necessary foundations to develop an integrated optics platform, which enables strong interaction of non-Si materials with silicon photonics devices to overcome the material limitations of silicon. Further, we have investigated the studied devices to address critical limitations in silicon photonics, (i) non-birefringence, (ii) non-reciprocal effects, and (iii) low loss waveguides.

4.2 Outlook

Silicon photonics and in general CMOS compatible integrated optical platforms hold promise for the future of nanoelectronics. Today’s integrated silicon photonics platforms enable high speed modulators, photodetectors and various passive functionalities on SOI wafers [74]. Such technologies are undergoing various trials for telecom, datacom and sensing applications. However, silicon photonics still faces various challenges, prominently– thermal stabilization, integrated light sources, very low loss waveguides, CMOS process limitations for nanophotonics and a maturing design flow. Typical CMOS process limitations for nanophotonics include inter-layer misalignment tolerance, etch process induced sidewall roughness and phase error noise, and, non critical dimension (CD) device biasing due to optical lithography etc. Currently, design based approaches to offset process limitations are necessary. Locally thick waveguides to reduce sidewall induced scattering, thus minimizing device insertion loss may be used. Due to optical lithography constraints corrective geometric biases have to be applied to a vast number of devices to obtain targeted device geometries. State-of-the-art fabrication for photonics on the 300 mm wafer based CMOS pilot line has shown considerably lower waveguide loss (<1 dB/cm for 450 nm wide Si wire) and low phase error noise. However, such processes are expensive and require "economics of scale" to become prevalent. Furthermore, the design flow infrastructure to support access to fabless technologies is still in an early stage. Design tools and fabrication facilities provide process design kits (PDKs) to enable easier access to advanced CMOS based silicon photonics technologies. These PDKs include tested component with known performance and limited circuits, such as 4/8 channel AWGs, travelling wave Mach-Zehnder interferometer (MZI) modulators, ring resonator based PIN depletion modulator, photodiodes etc. Design verification is provided through design rule check (DRC), design for manufacturability (DfM), layout versus schematic (LVS) and optical proximity correction (OPC).

Silicon photonics is a rapidly maturing technology with wide range of applications. Its massive adoption continues to be foreseen and is widely accepted as imminent [75].

References

[1] K. Jain and G. W. Pratt, “Optical transistor,” *Applied Physics Letters*, vol. 28, no. 12, pp. 719–721, 1976.

[2] R. Soref and J. Lorenzo, “Single-crystal silicon: a new material for 1.3 and 1.6 um integrated-optical components,” *Electronics Letters*, vol. 21, pp. 953–954(1), October 1985.

[3] D. Miller, “Optical interconnects to silicon,” *IEEE Journal of Selected Topics in Quantum Electronics*, vol. 6, pp. 1312–1317, Nov 2000.

[4] E. A. J. Marcatili, “Dielectric rectangular waveguide and directional coupler for integrated optics,” *Bell System Technical Journal*, vol. 48, no. 7, pp. 2071–2102, 1969.

[5] R. Soref, “The past, present, and future of silicon photonics,” *Appl. Opt.*, vol. 12, no. 6, pp. 1678–1687, 2006.

[6] C. Gunn, “CMOS photonics for high-speed interconnects,” *Micro, IEEE*, vol. 26, pp. 58–66, March 2006.

[7] H. B. Briggs, “Infra-red absorption in silicon,” *Phys. Rev.*, vol. 77, pp. 727–728, Mar 1950.

[8] S. K. Selvaraja, G. Winroth, S. Locorotondo, G. Murdoch, A. Milenin, C. Delvaux, P. Ong, S. Pathak, W. Xie, G. Sterckx, G. Lepage, D. Van Thourhout, W. Bogaerts, J. Van Campenhout, and P. Absil, “193nm immersion lithography for high-performance silicon photonic circuits,” in *Proc. SPIE*, vol. 9052, pp. 90520F–90520F–9, 2014.

[9] W. Bogaerts and S. Selvaraja, “Compact single-mode silicon hybrid rib/strip waveguide with adiabatic bends,” *Photonics Journal, IEEE*, vol. 3, pp. 422–432, June 2011.

[10] V. R. Almeida, C. A. Barrios, R. R. Panepucci, and M. Lipson, “All-optical control of light on a silicon chip,” *Nature*, vol. 431, pp. 1081–1084, oct 2004.

[11] A. Liu, R. Jones, L. Liao, D. Samara-Rubio, D. Rubin, O. Cohen, R. Nicolaescu, and M. Paniccia, “A high-speed silicon optical modulator based on a metal-oxide-semiconductor capacitor,” *Nature*, vol. 427, pp. 615–618, feb 2004.

[12] J. Michel, J. Liu, and L. Kimerling, “High-performance Ge-on-Si photodetectors,” *Nature Photonics*, vol. 4, pp. 527–534, aug 2010.

[13] X. Zheng, D. Patil, J. Lexau, F. Liu, G. Li, H. Thacker, Y. Luo, I. Shubin, J. Li, J. Yao, P. Dong, D. Feng, M. Asghari, T. Pinguet, A. Mekis, P. Amberg, M. Dayringer, J. Gainsley, H. Moghadam, E. Alon, K. Raj, R. Ho, J. Cunningham, and A. Krishnamoorthy, “Ultra-efficient 10 Gb/s hybrid integrated silicon photonic transmitter and receiver,” *Opt. Express*, vol. 19, pp. 5172–5186, Mar 2011.

[14] L. Zimmermann, K. Voigt, G. Winzer, D. Wolansky, S. Geisler, H. Richter, and B. Tillack, “Silicon photonics front-end integration in high-speed 0.25um SiGe BiCMOS,” in *Group IV Photonics, Proceedings of 2008 5th IEEE International Conference on*, pp. 374–376, Sep 2008.

[15] “European nanoelectronics initiative advisory council.”

[16] P. P. Absil, P. De Heyn, P. Dumon, D. V. Thourhout, P. Verheyen, S. Selvaraja, G. Lepage, M. Pantouvaki, M. Rakowski, and J. Van Campenhout, “193nm immersion lithography for high-performance silicon photonic circuits,” in *Proc. SPIE 9010, Next-Generation Optical Networks for Data Centers and Short-Reach Links*, vol. 9010, 2014.

[17] D. Gallagher, “Fimmwave photonics simulation software, photon design,” 2014.

[18] V. R. Almeida, Q. Xu, C. A. Barrios, and M. Lipson, “Guiding and confining light in void nanostructure,” *Opt. Lett.*, vol. 29, pp. 1209–1211, Jun 2004.

[19] T. Alasaarela, D. Korn, L. Alloatti, A. Säynätjoki, A. Tervonen, R. Palmer, J. Leuthold, W. Freude, and S. Honkanen, “Reduced propagation loss in silicon strip and slot waveguides coated by atomic layer deposition,” *Opt. Express*, vol. 19, pp. 11529–11538, Jun 2011.

[20] L. Pavesi and D. J. Lockwood, *Silicon Photonics II: Components and Integration*. Springer-Verlag, 2011.

[21] K. K. Lee, D. R. Lim, H.-C. Luan, A. Agarwal, J. Foresi, and L. C. Kimerling, “Effect of size and roughness on light transmission in a Si-SiO2 waveguide: Experiments and model,” *Applied Physics Letters*, vol. 77, no. 11, pp. 1617–1619, 2000.

[22] F. Payne and J. Lacey, “A theoretical analysis of scattering loss from planar optical waveguides,” *Optical and Quantum Electronics*, vol. 26, no. 10, pp. 977–986, 1994.

[23] K. Yamada, “Silicon photonic wire waveguides: Fundamentals and applications,” in *Silicon Photonics II* (D. J. Lockwood and L. Pavesi, eds.), vol. 119 of *Topics in Applied Physics*, pp. 1–29, Springer Berlin Heidelberg, 2011.

[24] M. Gnan, “Fabrication of low-loss photonic wires in silicon-on-insulator using hydrogen silsesquioxane electron-beam resist,” *Electronics Letters*, vol. 44, pp. 115–116(1), January 2008.

[25] M. Borselli, T. J. Johnson, C. P. Michael, M. D. Henry, and O. Painter, “Surface encapsulation for low-loss silicon photonics,” *Applied Physics Letters*, vol. 91, no. 13, 2007.

[26] S. Spector, M. W. Geis, D. Lennon, R. C. Williamson, and T. M. Lyszczarz, “Hybrid multi-mode/single-mode waveguides for low loss,” in *Optical Amplifiers and Their Applications/Integrated Photonics Research*, p. IThE5, Optical Society of America, 2004.

[27] S. Sridaran and S. A. Bhave, “Nanophotonic devices on thin buried oxide silicon-on-insulator substrates,” *Opt. Express*, vol. 18, pp. 3850–3857, Feb 2010.

[28] T. Barwicz, C. W. Holzwarth, P. T. Rakich, M. A. Popovic, E. P. Ippen, and H. I. Smith, “Optical loss in silicon microphotonic waveguides induced by metallic contamination,” *Applied Physics Letters*, vol. 92, no. 13, 2008.

[29] E. Dulkeith, F. Xia, L. Schares, W. M. J. Green, and Y. A. Vlasov, “Group index and group velocity dispersion in silicon-on-insulator photonic wires,” *Opt. Express*, vol. 14, pp. 3853–3863, May 2006.

[30] Y.-F. Ma, M.-J. Sung, and D.-W. Huang, “Controlling the polarization dependence of dual-channel directional couplers formed by silicon-on-insulator slot waveguides,” *Appl. Opt.*, vol. 49, pp. 6979–6985, Dec 2010.

[31] J. V. Galan, P. Sanchis, J. Garcia, J. Blasco, A. Martinez, and J. Marti, “Study of asymmetric silicon cross-slot waveguides for polarization diversity schemes,” *Appl. Opt.*, vol. 48, pp. 2693–2696, May 2009.

[32] X. Tu, S. Ang, A. Chew, J. Teng, and T. Mei, “An ultracompact directional coupler based on GaAs cross-slot waveguide,” *Photonics Technology Letters, IEEE*, vol. 22, pp. 1324–1326, Sept 2010.

[33] H. Lira, Z. Yu, S. Fan, and M. Lipson, “Electrically driven nonreciprocity induced by interband photonic transition on a silicon chip,” *Phys. Rev. Lett.*, vol. 109, p. 033901, Jul 2012.

[34] H. Dotsch, N. Bahlmann, O. Zhuromskyy, L. M. Hammer, R. Gerhardt, and P. Hertel, “Applications of magneto-optic waveguides in integrated optics: review,” *J. Opt. Soc. Am. B*, vol. 22, no. 1, pp. 240–253, 2005.

[35] T. R. Zaman, X. Guo, and R. J. Ram, “Semiconductor waveguide isolators,” *Journal of Lightwave Technology*, vol. 26, no. 2, pp. 291–301, 2008.

[36] Y. Okamura, T. Negami, and S. Yamamoto, “Integrated optical isolator and circulator using nonreciprocal phase shifters: a proposal,” *Appl. Opt.*, vol. 23, no. 11, pp. 1886–1889, 1984.

[37] R. L. Espinola, T. Izuhara, M.-C. Tsai, J. R. M. Osgood, and H. Dotsch, “Magneto-optic nonreciprocal phase shift in garnet/silicon-on-insulator waveguides,” *Opt. Lett.*, vol. 29, no. 9, pp. 941–943, 2004.

[38] H. Yokoi, T. Mizumoto, and Y. Shoji, “Optical nonreciprocal devices with a silicon guiding layer fabricated by wafer bonding,” *Appl. Opt.*, vol. 42, no. 33, pp. 6605–6612, 2003.

[39] S. Y. Sung, X. Qi, and B. J. H. Stadler, “Integration of magneto-optic garnet waveguides and polarizers for optical isolators,” *Conf. Lasers and Electro-Optics / Quantum Electronics and Laser Science Tech. Dig., CThM4*, 2008.

[40] L. Bi, J. Hu, L. C. Kim, and C. A. Ross, “Fabrication and characterization of As2S3/Y3Fe5O12 and Y3Fe5O12/SOI strip-loaded waveguides for integrated optical isolator applications,” *Proc. SPIE*, vol. 7604, 2010.

[41] P. Gangopadhyay, R. Voorakaranam, A. Lopez-Santiago, S. Foerier, J. Thomas, R. A. Norwood, A. Persoons, , and N. Peyghambarian, “Faraday rotation measurements on thin films of regioregular alkyl-substituted polythiophene derivatives,” *J. Phys. Chem. C*, vol. 112, no. 21, pp. 8032–8037, 2008.

[42] A. Lopez-Santiago, P. Gangopadhyay, J. Thomas, R. A. Norwood, A. Persoons, , and N. Peyghambarian, “Faraday rotation in magnetite-polymethylmethacrylate core-shell nanocomposites with high optical quality,” *Appl. Phys. Lett.*, vol. 95, no. 14, pp. 143302–1, 143302–3, 2009.

[43] J. Chilwell and I. Hodgkinson, “Thin-films field-transfer matrix theory of planar multilayer waveguides and reflection from prism-loaded waveguides,” *J. Opt. Soc. Am. A*, vol. 1, no. 7, pp. 742–753, 1984.

[44] J. T. Robinson, K. Preston, O. Painter, and M. Lipson, “First-principle derivation of gain in high-index-contrast waveguides,” *Opt. Express*, vol. 16, no. 21, pp. 16659–16669, 2008.

[45] H. Yokoi, T. Mizumoto, N. Shinjo, N. Futakuchi, N. Kaida, and Y. Nakano, “Feasibility of integrated optical isolator with semiconductor guiding layer fabricated by wafer direct bonding,” *IEE Proc.-Optoelectron.*, vol. 146, no. 2, pp. 105–110, 1999.

[46] P. Mullner and R. Hainberger, “Optical characteristics of v-groove waveguide structures,” *Proc. SPIE 7220*, 2009.

[47] R. Adair, L. L. Chase, and S. A. Payne, “Nonlinear refractive index of optical crystals,” *Phys. Rev. B*, vol. 39, pp. 3337–3350, Feb 1989.

[48] T. Alasaarela, A. Säynätjoki, T. Hakkarainen, and S. Honkanen, “Feature size reduction of silicon slot waveguides by partial filling using atomic layer deposition,” *Optical Engineering*, vol. 48, no. 8, pp. 080502–080502–3, 2009.

[49] T. Pilvi, E. Puukilainen, U. Kreissig, M. Leskela, and M. Ritala, “Atomic layer deposition of MgF2 thin films using TaF5 as a novel fluorine source,” *Chemistry of Materials*, vol. 20, no. 15, pp. 5023–5028, 2008.

[50] L. Karvonen, A. Säynätjoki, Y. Chen, H. Jussila, J. Ronn, M. Ruoho, T. Alasaarela, S. Kujala, R. A. Norwood, N. Peyghambarian, K. Kieu, and S. Honkanen, “Enhancement of the third-order optical nonlinearity in ZnO/Al2O3 nanolaminates fabricated by atomic layer deposition,” *Applied Physics Letters*, vol. 103, pp. 1–4, 2013.

[51] T. Alasaarela, L. Karvonen, A. Säynätjoki, H. Jussila, S. Mehravar, R. A. Norwood, N. Peyghambarian, K. Kieu, I. Tittonen, and H. Lipsanen, “High quality crystallinity controlled ALD TiO2 for waveguiding applications,” *Opt. Lett.*, vol. 38, pp. 3980–3983, 2013.

[52] P. Sanchis, J. Blasco, A. Martinez, and J. Marti, “Design of Silicon-Based Slot Waveguide Configurations for Optimum Nonlinear Performance,” *Journal of Lightwave Technology*, vol. 25, no. 5, pp. 1298–1305, 2007.

[53] F. Dell’Olio and V. M. Passaro, “Optical sensing by optimized silicon slot waveguides,” *Opt. Express*, vol. 15, pp. 4977–4993, Apr 2007.

[54] A. Säynätjoki, L. Karvonen, A. Khanna, T. Alasaarela, A. Tervonen, and S. Honkanen, “Silicon slot waveguides for nonlinear optics,” *Proc. SPIE 7212*, 2009.

[55] N. Daldosso and L. Pavesi, “Nanosilicon photonics,” *Laser and Photonics Reviews*, vol. 3, no. 6, pp. 508–534, 2009.

[56] R. Spano, N. Daldosso, M. Cazzanelli, L. Ferraioli, L. Tartara, J. Yu, V. Degiorgio, E. Giordana, J. M. Fedeli, and L. Pavesi, “Bound electronic and free carrier nonlinearities in silicon nanocrystals at 1550nm,” *Opt. Express*, vol. 17, pp. 3941–3950, Mar 2009.

[57] K. Worhoff, J. D. B. Bradley, F. Ay, D. Geskus, T. Blauwendraat, and M. Pollnau, “Reliable low cost fabrication of low loss Al2O3-Er waveguides with 5.4db optical gain,” *IEEE Journal of Quantum Electronics*, vol. 45, pp. 454–461, May 2009.

[58] M. Tiitta and L. Niinistö, “Volatile metal beta-diketonates: ALE and CVD precursors for electroluminescent device thin films,” *Chemical Vapor Deposition*, vol. 3, no. 4, pp. 167–182, 1997.

[59] J. T. Robinson, K. Preston, O. Painter, and M. Lipson, “First-principle derivation of gain in high-index-contrast waveguides,” *Opt. Express*, vol. 16, pp. 16659–16669, Oct 2008.

[60] K. Ikeda, R. E. Saperstein, N. Alic, and Y. Fainman, “Thermal and Kerr nonlinear properties of plasma-deposited silicon nitride/ silicon dioxide waveguides,” *Opt. Express*, vol. 16, pp. 12987–12994, Aug 2008.

[61] A. Gondarenko, J. S. Levy, and M. Lipson, “High confinement micron-scale silicon nitride high Q ring resonator,” *Opt. Express*, vol. 17, pp. 11366–11370, Jul 2009.

[62] F. Morichetti, A. Melloni, M. Martinelli, R. G. Heideman, A. Leinse, D. H. Geuzebroek, and A. Borreman, “Box-shaped dielectric waveguides: A new concept in integrated optics,” *Journal of Lightwave Technology*, vol. 25, pp. 2579–2589, Sep 2007.

[63] N. Daldosso, M. Melchiorri, F. Riboli, M. Girardini, G. Pucker, M. Crivellari, P. Bellutti, A. Lui, and L. Pavesi, “Comparison among various Si3N4 waveguide geometries grown within a CMOS fabrication pilot line,” *Journal of Lightwave Technology*, vol. 22, pp. 1734–1740, July 2004.

[64] M. Melchiorri, N. Daldosso, F. Sbrana, L. Pavesi, G. Pucker, C. Kompocholis, P. Bellutti, and A. Lui, “Propagation losses of silicon nitride waveguides in the near-infrared range,” *Applied Physics Letters*, vol. 86, no. 12, 2005.

[65] J. S. Levy, A. Gondarenko, M. A. Foster, A. C. Turner-Foster, A. L. Gaeta, and M. Lipson, “CMOS-compatible multiple-wavelength oscillator for onchip optical interconnects,” *Nature Photonics*, vol. 4, pp. 1749–4885, Jan 2010.

[66] L. Razzari, D. Duchesne, M. Ferrera, R. Morandotti, S. Chu, B. E. Little, and D. J. Moss, “CMOS-compatible integrated optical hyper-parametric oscillator,” *Nature Photonics*, vol. 4, pp. 1749–4885, Jan 2010.

[67] S. Romero-García, F. Merget, F. Zhong, H. Finkelstein, and J. Witzens, “Silicon nitride CMOS-compatible platform for integrated photonics applications at visible wavelengths,” *Opt. Express*, vol. 21, pp. 14036–14046, Jun 2013.

[68] I. Goykhman, B. Desiatov, and U. Levy, “Ultrathin silicon nitride microring resonator for biophotonic applications at 970 nm wavelength,” *Applied Physics Letters*, vol. 97, no. 8, 2010.

[69] S. Romero-García, F. Merget, F. Zhong, H. Finkelstein, and J. Witzens, “Silicon nitride CMOS-compatible platform for integrated photonics applications at visible wavelengths,” *Opt. Express*, vol. 21, pp. 14036–14046, Jun 2013.

[70] A. Gorin, A. Jaouad, E. Grondin, V. Aimez, and P. Charette, “Fabrication of silicon nitride waveguides for visible-light using PECVD: a study of the effect of plasma frequency on optical properties,” *Opt. Express*, vol. 16, pp. 13509–13516, Sep 2008.

[71] J. N. Milgram, J. Wojcik, P. Mascher, and A. P. Knights, “Optically pumped Si nanocrystal emitter integrated with low loss silicon nitride waveguides,” *Opt. Express*, vol. 15, pp. 14679–14688, Oct 2007.

[72] M. Häyrinen, M. Roussey, V. Gandhi, M. Kuittinen, and S. Honkanen, “New approach to fabricate low-loss titanium dioxide waveguides with electron beam lithography and atomic layer deposition,” *Advanced Photonics 2013, paper IT2A.5, OSA Technical Digest (online)*, 2013.

[73] A. Subramanian, S. Selvaraja, P. Verheyen, A. Dhakal, K. Komorowska, and R. Baets, “Near-infrared grating couplers for silicon nitride photonic wires,” *Photonics Technology Letters*, vol. 24, no. 8, pp. 1700–1703, 2012.

[74] C. Das and D. Bode, “Europractice-IC.”

[75] E. Mounier and C. Troadec, “Silicon photonics Yole development report 2014.”

Aalto-DD 74/2015

CMOS integrated optics will bring light on a microprocessor chip. This will allow ultra-high speed and large bandwidth for telecommunications, datacenters, and consumer cables. The communication bandwidth will increase all the way from datacenters to the user. CMOS integrated optics is also useful for applications such as sensing for healthcare and environment. These sensors provide high accuracy and reproducibility due to the well-established CMOS processing techniques. Such products are not far in the future since they are based on processes used to make billions of electronic chips today.

In this thesis we propose new CMOS integrated optic waveguides. These waveguides are useful for sensing and communications since they guide light in the low-index material regions. We show that, by a proper design, the material asymmetry limitation of CMOS integrated optics can be solved. We also demonstrate unprecedented recovery of a high loss waveguide through a CMOS based post-processing technique.

9 789526 062242

ISBN 978-952-60-6224-2 (printed)
ISBN 978-952-60-6225-9 (pdf)
ISSN-L 1799-4934
ISSN 1799-4934 (printed)
ISSN 1799-4942 (pdf)

Aalto University
School of Electrical Engineering
Department of Micro and Nanosciences
www.aalto.fi